FOURIER TRANSFORM INFRARED, RAMAN AND ELECTRON SPIN RESONANCE SPECTROSCOPY OF MATRIX ISOLATED SPECIES

By

HEATHER ANN WEIMER

A DISSERTATION PRESENTED TO THE GRADUATE SCHOOL
OF THE UNIVERSITY OF FLORIDA IN PARTIAL FULFILLMENT
OF THE REQUIREMENTS FOR THE DEGREE OF
DOCTOR OF PHILOSOPHY

UNIVERSITY OF FLORIDA

1998

TO MY PARENTS AND GRANDPARENTS

AKNOWLEDGEMENTS

The author wishes to first extend thanks to Professor William Weltner, Jr., whose support and encouragement were instrumental in inspiring this journey and without whom the road would have been unsurpassable. The knowledge he has imparted and patience he has displayed were vital to completing this work. A deep debt of gratitude is owed to Dr. Richard Van Zee. His guidance and help have made all of this possible. Thanks must also be extended to Professor David Powell who provided not only the introduction to spectroscopy, but whose general chemistry class began all this.

Credit is also due to the wonderful support staff in the Department of Chemistry. Without the aid of these people, the glass would have remained broken, the electronics would have been dark and the flanges would never have existed. Special thanks go out to Lori Clark, Steve Miles and Larry Hartley, all of whom have provided endless assistance and tolerance with an often frantic graduate student.

Thanks are also given to Dr. San Li, Troy D. Halvorsen, Dr. Aaron P. Williams, Dr. Marian Szczesniak, Dr. Christine M. Wehlburg, Dr. Lori Kornberg, Dr. Tom Hayes, Debby Tindell, Leslie Anthony King, Ted O'Brien and Johnny Evans. Without the advice and friendship of these colleagues, surviving the last four years would have been impossible.

The author must also acknowledge the National Science Foundation (NSF) and the Center for Chemical Physics for the financial support necessary to complete this work.

TABLE OF CONTENTS

Page

AKNOWLEDGEMENTS iii

LIST OF TABLES vii

LIST OF FIGURES viii

ABSTRACT xii

CHAPTERS

1 MATRIX ISOLATION 1

2 INFRARED AND RAMAN THEORY 7

3 THE INFRARED CHARACTERIZATION OF THE LINEAR ISOMERS OF C_2N_2 20

    Introduction 20
    Experimental 21
    Results and Discussion 26

4 NORMAL CORDINATE ANALYSIS................ 34

5 DIDEHYDROGENATED DERIVATIVES OF POLYCYCLIC AROMATIC HYDROCARBONS 45

    Introduction 45
    Experimental 48
    2,3-Naphthyne 52
    1,2-Naphthyne 59
    Comparison of the 2,3 and 1,2-Naphthyne Molecules 65
    Photolysis of 1,2,4,5-Benzenetetracarboxylic Dianhydride ... 71

6 MATRIX ISOLATION FT-RAMAN SPECTROSCOPY ... 80

Introduction ... 80
General Apparatus ... 86
Individual Setup and Results ... 89
Discussion ... 102

7 ELECTRON SPIN RESONANCE THEORY ... 111

Introduction ... 111
Atomic Interactions in a Magnetic Field ... 112
Nuclear Hyperfine Splitting ... 114
The Effect of Molecular Orientation ... 120

8 SODIUM DIMER CATION ... 124

Introduction ... 124
Experimental ... 125
Results ... 131
Analysis ... 137

9 CONCLUSIONS ... 142

APPENDIX A SECOND ORDER PERTURBATION TREATMENT OF Na_2^+ ... 144

REFERENCES ... 146

BIOGRAPHICAL SKETCH ... 158

LIST OF TABLES

Table Page

3-1 Observed fundamental band positions of isocyanogen and diisocyanogen in solid argon at 4K 29

3-2 Observed and calculated isotopic shifts for isocyanogen and diisocyanogen 30

3-3 Force constants for isocyanogen as calculated using normal coordinate analysis. 31

4-1 The **f** matrix elements for cyanogen stretches 41

4-2 **U** matrix elements for σ_g vibrations 42

5-1 Observed fundamental band positions and intensities of 2,3-naphthyne in solid neon, argon and krypton as compared to predicted values ... 57

5-2 Observed fundamental band positions and intensities of 1,2-naphthyne in solid argon and neon as compares to predicted values 62

5-3 Comparison of 1,2-naphthyne to 2,3-naphthyne band positions as observed in solid neon. 67

8-1 The observed line positions of the ESR spectrum of Na_2^+ in solid neon compared to the calculated values. 133

8-2 Non-zero spin matrix elements numbered as indicated in figure 8-5. 136

8-3 Derived magnetic parameters for Na_2^+ in solid neon at 4K. 139

LIST OF FIGURES

Figure Page

2-1 Scattering phenomina 15

2-2 FT-Raman spectrum of sulfer showing Stokes and Anti-Stokes Raman scattering 16

3-1 Production of CN dimers by corona discharge 22

3-2 Cutaway side schematic of sample chamber. 24

3-3 Corona discharge apparatus. 25

3-4 FTIR spectrum of C_2N_2 in argon at 4K taken at 2 cm^{-1} resolution. (A) $^{12}C_2{}^{14}N_2$, (B) $^{13}C_2{}^{14}N_2$, (C) $^{12}C_2{}^{15}N_2$. 27

3-5 FTIR spectrum of C_2N_2 bending region in argon at 4K taken at 2 cm^{-1} resolution. (A) $^{12}C_2{}^{14}N_2$, (B) $^{13}C_2{}^{14}N_2$, (C) $^{12}C_2{}^{15}N_2$. 28

4-1 Normal modes of cyanogen. a) Assignment of variables b) Symmetry and motion of individual modes. 38

5-1 Cross-section of sample chamber and cryostat. 50

5-2 2,3-naphthalene anhydride (bands projected down) and 2,3-naphthyne (*bands) in solid argon and neon. 53

5-3 2,3-naphthalene anhydride (bands projected down) and 2,3-naphthyne (*bands) in solid argon and neon. 54

5-4 2,3-naphthalene anhydride (bands projected down) and 2,3-naphthyne (*bands) in solid argon and neon. 55

5-5 1,2-naphthalene anhydride (bands projected down) and 1,2-naphthyne (*bands) in solid neon. 61

5-6 The FTIR spectrum of the CO stretching region of a neon matrix containing CO and 1,2-naphthyne 64

5-7 The CO stretching region of and argon matrix containing CO and 1,2-naphthyne. A) Original deposition at 4K. B) After annealing to 32K. 66

5-8 Naphthyne isomers showing the relative positions of the remaining hydrogen atoms. 69

5-9 The FTIR spectrum of 1,2,4,5-benzeneteracarboxylic dianhydride in solid argon. A) Original sample. B) after photolysis. C) Following annealing to 32K. . 74

5-10 Possible products of the photolysis of 1,2,4,5-benzeneteracarboxylic dianhydride in solid argon. 75

5-11 The FTIR spectrum of 1,2,4,5-benzeneteracarboxylic dianhydride in solid krypton. A) Original sample. B) after photolysis. C) Following annealing to 45K. . 77

5-12 The FTIR spectrum of 1,2,4,5-benzeneteracarboxylic dianhydride in solid neon. A) Original sample. B) after photolysis. C) Following annealing to 6K. .. 78

6-1 The Michelson interferometer 83

6-2 The interferogram (A)and resulting transformed spectrum (B) of a polychromatic light source. 85

6-3 FT-Raman cryostat, side view. 87

6-4 FT-Raman spectrum of 0.1% cyanogen in solid krypton . 90

6-5 Spectrum of an argon matrix with trace impurities deposited with vacuum UV photolysis. 93

6-6 The spectrum of a nitrogen matrix containing trace impurities following photolysis with vacuum UV radiation. 94

6-7 The spectrum of xenon containing trace impurities including oxygen, following photolysis with vacuum UV radiation 95

6-8 The effects of temperature on the spectrum of a krypton matrix containing trace impurities. 96

6-9 Windowed microwave discharge tube. 100

6-10 The spectrum of 0.1% oxygen in solid krypton at 12K 103

6-11 The comparison of 0.1% oxygen in solid krypton (A), to 0.1% oxygen in solid argon (B). Both spectra are taken at 12K. 105

6-12 The spectrum of 1% oxygen in solid argon at 12K 106

7-1 The electronic Zeeman splitting observed for a free electron in a magnetic field, H_o. 115

7-2 The splitting of electronic Zeeman levels observed for an I=3/2 atom. 117

8-1 ESR cryostat, side-view schematic. 126

8-2 Sample preparation area, side-view cross-section. .. 128

8-3 The ESR spectrum of Na_2^+ in solid neon. 130

8-4 Expanded view of Na_2^+ in neon showing low field perpendicular lines. 132

8-5 The spin matrix for I=3/2, S=1/2. The non-zero elements are given in table 8-2. 135

8-6 Energy level diagram for perpendicular ESR transitions of Na_2^+. Arrows indicate predicted ESR transitions, while lines represent the energy levels involved. 138

Abstract of Dissertation Presented to the Graduate School
of the University of Florida in Partial Fulfillment of the
Requirements for the Degree of Doctor of Philosophy

FOURIER TRANSFORM INFRARED, RAMAN AND ELECTRON SPIN RESONANCE SPECTROSCOPY OF MATRIX ISOLATED SPECIES

By

Heather Ann Weimer

August 1998

Chairman: Professor William Weltner, Jr.
Major Department: Chemistry

Three linear isomers of natural abundance C_2N_2 and the carbon 13 and nitrogen 15 labeled isotopomers have been isolated in argon matrices at 10K. The spectra of this system were obtained using Fourier transform infrared spectroscopy (FTIR). The resulting spectra were assigned through comparison to earlier work and to *ab initio* calculations. Normal coordinate analysis was then used to obtain force constants for isocyanogen.

FTIR spectra were obtained for two different didehydrogenated derivatives of naphthalene, 1,2-naphthyne and 2,3-naphthyne, in rare gas matrices. This is the first vibrational characterization of polycylic aromatic hydrocarbons derivatives of this type. The FTIR spectra of the photolysis products of 1,2,4,5-benzeneteracarboxylic dianhydride were obtained in neon, argon and krypton. The effects of photolysis in different matrix environments was investigated.

The technique of FT-Raman spectroscopy was coupled to matrix isolation. This technique has proven effective for stable molecules with concentrations as small as 0.1%. Problems have arisen with oxygen impurities, which are resonantly excited by the 1064cm^{-1} Nd:YAG laser used here. Additional challenges arise in systems where ultraviolet photolysis produces fluorescent impurities. While it has not been possible to obtain matrix isolation FT-Raman spectra of these systems, they merit further study by other means.

The electron spin resonance spectrum of Na_2^+ was obtained in a neon matrix. This $^2\Sigma$ molecule was found to possess about 28% pσ bonding character in contrast with theoretical predictions found in the literature.

CHAPTER 1
MATRIX ISOLATION

The matrix isolation technique was introduced in 1954 by G.C. Pimentel.[1] This method provides a means to hold reactive or transient species for investigation by a variety of experimental methods. It has been applied to a large number of molecules and free radicals, including species thought to be of astrophysical importance. Matrix isolation involves co-condensing the reactive species with a sufficient excess of another substance, usually inert, as to provide isolation and prevent interaction of the species under study. The excess substance or matrix is carefully chosen in each experiment for its physical properties. The species to be studied can either be generated before condensation by a wide range of techniques, or in situ through photolysis of a trapped precursor molecule. The choice of substrate on which the matrix is condensed is usually determined by the spectroscopic technique used to study the isolated molecules.

Matrix isolation experiments are performed at low temperatures where the matrix is rigid, or where there is very little thermal energy to allow diffusion, rearrangement or dissociation of the trapped species. Additionally, at these temperatures molecules are in their ground electronic and vibrational states. The rotation of all but the smallest of molecules, such as hydrogen and water, will also be prevented. These factors can greatly simplify data interpretation. It should be noted however, that there is a concomitant loss of information as a result of these constraints.

Matrix isolation is often used to approximate gas phase conditions. The matrix gas is then chosen to be inert and relatively non-perturbing. It must be optically transparent to the spectroscopic technique being used to study the isolated molecules, and a rigid solid at temperatures accessible to the apparatus. A matrix gas becomes more perturbing as its polarizablity increases and as its shape becomes more irregular. Common choices are therefore the noble gases; xenon, krypton, argon, neon; and homonuclear diatomics such as nitrogen and hydrogen. Among the noble gases, a neon matrix provides the least perturbing environment and xenon the most.

The molecule to be studied will be trapped as an impurity within the crystal lattice of the host gas. It is possible for large molecules to be trapped in different orientations or sites within the matrix. The use of several matrix gases in an experiment provides a means to evaluate the effects of the environment on the species under study. Additionally, it is often desirable to warm or anneal the matrix, to remove strain in the crystal lattice and allow the relaxation and migration of small species within the matrix. Often the splitting of lines resulting from matrix sites can be eliminated in this way. The low melting point of neon and hydrogen make this difficult, so argon, while larger and slightly more perturbing, is the most commonly used matrix material.

Matrix isolation can also be used to examine reactions of species within the matrix. This can be effected through the choice of a reactive matrix material such as a hydrocarbon, or through doping an inert gas with a known percentage of a reactive species. Reactions can be induced by warming of the matrix to allow migration of atoms and small molecules, or through photolysis.

Since the matrix gases described above are solids only at cryogenic temperatures, it is necessary to perform these experiments in a relatively high vacuum apparatus, with normal deposition pressures falling in the range of 10^{-6} torr. This is necessary to minimize the condensation of atmospheric contaminates, and also to allow the successful cooling of the deposition surface to temperatures as low as 1.8K, depending on the requirements of the specific matrix gas being used. Methods of cooling include the use of closed cycle helium refrigerators and direct cooling with liquid helium. The choice of cooling method is based on the minimum temperature desired and on cost effectiveness. Both methods are used in this work and will be described later.

Techniques that have been used to generate species for study by matrix isolation can be divided into two categories. First are those which are used prior to condensation, including laser vaporization, pyrolysis, sublimation and high voltage discharges. The second are those that are used in situ such as photolysis or bombardment techniques. The choice of method is determined by each system to be studied. A detailed description of methods used in this work can be found in the chapters describing the individual experiments.

The substrate on which the matrix is condensed will vary according to the requirements of the measurement to be performed. In all cases the support chosen must have a high enough thermal conductivity to allow efficient cooling. It is also advantageous to have a multifaceted substrate which will allow matrices to be deposited on several faces or surfaces before the system must be warmed to room temperature for cleaning. Common substrates used in infrared measurements include alkali halide windows such as cesium iodide and polished metal surfaces such as platinum and gold. Raman measurements have been performed on the widest rage of substrates, including aluminum, brass, stainless steel sapphire and those already mentioned. Magnetic resonance techniques have relied on copper and sapphire rods, while visible and ultraviolet measurements allow the use of quartz windows. Some researchers have developed systems that allow more than one type of measurement to be performed on the same matrix, further complicating the choice of conditions.

While matrix isolation is a powerful technique it is not without disadvantages. There always exists some perturbation of the molecule by the matrix. This will show up as a shift in line positions. Some transitions, which are forbidden to the isolated species, can become allowed through distortion of the molecule by the surrounding environment. This is especially true for large and highly polarizable molecules. Care must be taken to study the molecule in several matrices and under a variety of conditions to correctly interpret the spectra obtained.

Additional complications can arise when coupling matrix isolation with spectroscopic techniques of lesser sensitivity. In the particular case of Raman spectroscopy the limits of detection are such that the concentration of the reactive species necessary for detection may be high enough that effective isolation can often not be achieved. As a result the observed spectra contain concentration dependent perturbations and must be interpreted with even more care.

Matrix isolation is an established technique, which has been applied to a wide range of experimental methods. There exist several review articles and books relating specific applications and details too numerous to be mentioned in this work.[1-12]

CHAPTER 2
INFRARED AND RAMAN THEORY

Spectroscopy measures the interaction of electromagnetic radiation with matter. The type of interactions observed will be dependent on the energy of the incident radiation and on the structure, geometry and nature of chemical bonds in the molecule being excited. There are three types of transitions observable with optical spectroscopy: rotation, vibration and electronic. The spectra obtained show that there are specific, quantized energies for each individual transition, with an associated observable intensity. These results cannot be predicted or interpreted without understanding the quantum mechanical description of these processes. It is impossible to provide a detailed treatment of this subject here, so only those results of importance to the work presented in this dissertation will be mentioned. The reader is referred to one of the numerous texts available.[13-15]

It is possible to write a function that contains all of the information about the system being investigated. Known as the wave function Ψ, from this the observable properties of the system can be expressed as a function of time. There also exists an operator corresponding to all observable properties of the system; these can be combined to give the time dependent Schrödinger equation

$$H\Psi(t) = E\Psi(t) \tag{1}$$

The Hamiltonian operator, H, contains terms corresponding to the kinetic and potential energy of the system and how they develop over time. When this acts on the appropriate wave function the result is a set of eigenvalues corresponding to the energy E of the molecule in its different states.

It is a good first approximation to consider the energies of vibrational, rotational and electronic states as independent of one another. The total energy of a molecule is the sum of the energies contained in each mode. Thus the overall wave function can be written as the product of the wave functions for each individual contribution.

$$\psi = \Psi_{vib}\,\Psi_{rot}\,\Psi_{el} \tag{2}$$

The present work deals primarily with the vibrational component of equation 2. The goal is to develop the correct form of the wave function and then to be able to solve the appropriate Schrödinger equation to arrive at the energy for a given state. For all but the simplest system, this must be done as an approximation. Even without an exact solution, a great deal of information can be derived from the form of the wave functions and the Hamiltonian operators used in each case.

First consider the vibrational wave function ψ_{vib}, and the associated potential and kinetic energy terms for a diatomic molecule. In the harmonic approximation, Hooke's law can be used to obtain an expression for the potential energy, V, of a vibration

$$V = \frac{1}{2}kx^2 \tag{3}$$

where k is a force constant describing the restoring force or strength of the chemical bond and x represents the displacement of the atoms from their equilibrium position. The kinetic energy, T, of the system is given by

$$T = \frac{p^2}{2\mu} \tag{4}$$

where p is the momentum and μ is the reduced mass if a diatomic molecule is involved. Combining these terms which describe the motion of the nuclei held together by the force of the bonding electrons, and setting x as the displacement from the rest position along the bond axis, gives the vibrational Schrödinger equation shown below.

$$\left\{-\frac{h^2}{8\pi^2\mu}\frac{d^2}{dx^2} + \frac{1}{2}kx^2\right\}\psi = E\psi . \tag{5}$$

A vibrational wave function of the general form

$$\psi_n(x) = N e^{-Ax^2/2} H_n\left(\sqrt{A}x\right) \qquad (6)$$

where $H_n\sqrt{A}x$ are Hermite polynomials, and N is a normalization factor, can be written for a harmonic diatomic molecule. The form of this wave function is very important in determining which transitions between vibrational energy levels are allowed. Hermite polynomials are developed from the recursion formula

$$\sqrt{A}x\ H(\sqrt{A}x) = nH_{v-1}(\sqrt{A}x) + \frac{1}{2}H_{v+1}(\sqrt{A}x) \qquad (7)$$

Where v is the quantum number (v = 0,1,2...) of the vibrational energy level, and

$$A = {}^{\nu\mu}\!/_{h} \qquad (8)$$

$$\nu = \frac{1}{2\pi}\sqrt{\frac{k}{\mu}} \qquad (9)$$

The resulting wave functions are orthonormal, the consequences of which will be discussed later. Substituting equation 6 into equation 7 and solving yields vibrational eigenvalues of the form

$$E_n = (n + \frac{1}{2})hc\bar{\nu}. \qquad (10)$$

where c is the speed of light and $\bar{\nu}$ is inverse frequency expressed in cm^{-1}.

Vibrational spectroscopy observes transitions between individual levels. Equation 10 allows the difference in energy of two levels to be calculated. The properties of the wavefunction described in equation 6 result in rules governing the probability of the occurrence of a given transition. The vibrational wave functions for the harmonic oscillator are orthonormal. This requires that

$$\int \psi_n \psi_m dx = \delta_{nm} \qquad (11)$$

Where n and m represent the energy levels involved in the transition. In the harmonic approximation, this integral will only be non-zero and the transition described allowed if (m-n)= ±1. Real molecules have anharmonic wavefunctions which allow transitions of $\Delta n = \pm 2, \pm 3, \ldots$. These higher order transitions are called overtones, and decrease in intensity with increasing Δn. The transition corresponding to $\Delta n = 1 \leftarrow 0$ for a given vibration is known as the fundamental. Transitions where $n_{lower} \neq 0$ are possible for vibrationally excited molecules.

In order for a molecule to absorb infrared radiation, it must have an electric dipole that is able to oscillate at the same frequency as incident light. It can be shown that the strength of an infrared absorption band is dependent on the electric dipole moment and how it changes with internuclear distance.[16,17] For the transition to be allowed, the dipole moment of that transition must be nonzero. The transition dipole moment is given by[17]

$$M_{nm} = \int \psi_n^* \mathbf{d} \psi_m dr \qquad (12)$$

where ψ_n is the upper energy level and ψ_m is the lower energy level of the transition. The variable **d** is the electric dipole operator and has the general form

$$d = \sum_i e_i x_i + \sum_i e_i y_i + \sum_i e_i z_i \qquad (13)$$

Where the index i represents individual atoms. The intensity of the transition is then given by the integral[17]

$$\int \psi_n^* (r - r_e) \;\; \psi_m dr \qquad (14)$$

where r and r_e are the actual internuclear and equilibrium internuclear distances. The actual infrared absorption intensities for polyatomic molecules are difficult to calculate; however, whether or not a band will be allowed is readily determined from the symmetry of the molecule. It is required that there be a net change in dipole moment as a result of the vibration in question. This can easily be determined when the symmetry of the molecule is known. Conversely, the presence or absence of absorption bands can allow insight into the symmetry of the molecule.

Infrared absorption is an example of a resonance technique; the frequency of absorbed light exactly matches the energy of the transition induced. While the Raman effect also arises from transitions between vibrational energy levels, conventional Raman scattering is an off-resonance technique. The incident and scattered radiation are of a different energy than the vibrational transition it interacts with. It is not unexpected then, that different selection rules apply. Infrared absorption requires a change in dipole moment, where as Raman scattering results from a change in the polarizability of the molecule. The intensity of Raman scattering is given as

$$I \propto \nu^4 I_0 \, \mathrm{f}(\alpha^2 \qquad (16)$$

where I_0 is the intensity of the exciting radiation, and α is the polarizability of the molecule. Qualitatively, the polarizability of a molecule is the tendency of the electron cloud to distort when an electric field is applied. The polarized state is more energetic than the non-polarized state, allowing for spontaneous emission to occur through relaxation. A molecule absorbs radiation of a frequency ν_0, raising it into a virtual state, which then decays to a stable state by the emission of a new photon. The excited molecule is able to return to its original state if it scatters a photon of the same energy as that absorbed. This process, known as Rayleigh scattering, is the most likely to occur. If the molecule does not return to the original state, but instead proceeds to a vibrationally excited state by emitting a photon of less energy than that absorbed, Stokes-Raman scattering is observed. The frequency of light emitted will be ($\nu_0 - \nu_{vib}$). A third scattering process is seen when a vibrationally excited molecule returns to the ground state by emitting a higher energy photon ($\nu_0 + \nu_{vib}$) than that absorbed. This is known as anti-Stokes-Raman scattering. Figure 2-1 shows these three processes in a schematic representation. Figure 2-2 shows the Raman spectrum of sulfur, displaying all three types of scattering. Observe that the Rayleigh scatter is suppressed by cut-off filters. In general, Rayleigh scatter is 10^3 times more intense than the Raman scatter observed. Note the relative intensity of corresponding Stokes and anti-Stokes bands. Since anti-Stokes scattering requires that the molecule be initially in an excited vibrational state, this ratio allows us to determine the relative population of vibrational energy levels before the absorption of the incident radiation. At room temperature there are a significant number of sulfur molecules in the n=1 excited state. Under the cryogenic conditions required for a matrix isolation experiment, anti-Stokes scattering will not be observed.

A significant enhancement of Raman scattering occurs when the incident radiation, ν_0, is at or near the energy of an electronic transition for the molecule being studied. This is known as Resonance Raman spectroscopy. Resonance

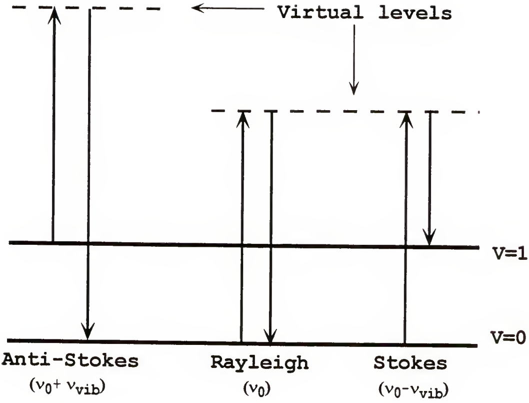

Figure 2-1 Scattering phenomena.

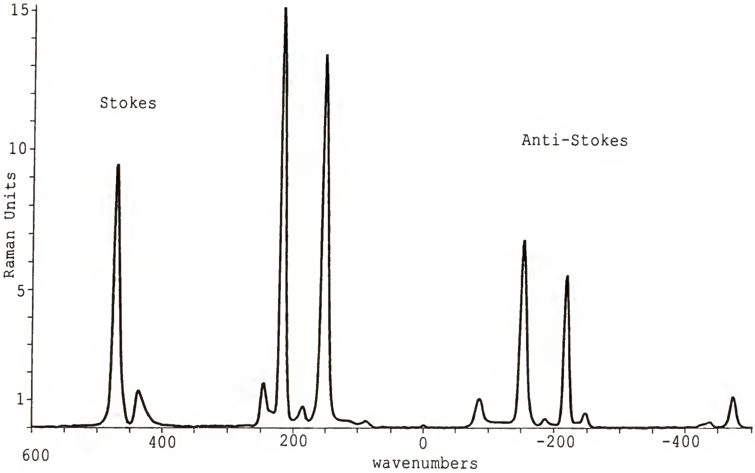

Figure 2-2 FT-Raman spectrum of sulfur showing Stokes and Anti-Stokes Raman scattering.

effects can cause distinct variation in the observed Raman spectrum of a molecule when the excitation energy is changed. Careful data interpretation is required when resonant conditions are suspected.

Infrared absorption and Raman scattering, as described above, are two complementary methods available to probe the vibrational energy levels and structure of a molecule. These two different techniques possess different selection rules, thus a vibrational mode forbidden to one technique may be allowed for the other. The observation of molecular vibrational frequencies can indicate the relative strength of chemical bonds. These selection rules governing the appearance of given vibrational modes in the spectrum often yield information about molecular geometry. All molecules have 3N total degrees of freedom, where N is the number of atoms in the molecule. Three are translational, and correspond to movement in the x, y, and z direction. A nonlinear molecule has three degrees of rotational freedom given by rotation around the x, y and z axes. Since rotation around the z axis has no effect for linear molecules, they only contain two rotational degrees of freedom. Therefore, nonlinear molecules have 3N-6 degrees of vibrational freedom and linear molecules 3N-5. Knowing the symmetry of a given molecule will allow us to predict which vibrations will cause a change in dipole moment and hence will be observable by infrared absorption. It is also possible to determine if a vibration will alter the polarizability of the molecule, causing it to be excitable using Raman scattering. The use of symmetry in the prediction and interpretation of vibrational spectroscopy has been summarized in several texts. The reader is referred to those works for the details and proof of the following results.[18,19]

Group theory allows complex polyatomic molecules to be classified by their symmetry properties. This scheme of grouping molecules containing common symmetry elements allows the development of tables listing the fundamental vibrational modes of each according to its symmetry. This is called the character table of a given point group. The symmetry of a vibration determines if the change in dipole moment or polarizability with vibration is non-zero, thus looking at the appropriate character table allows the infrared or Raman activity of a mode to be determined at a glance. The ground state vibrational wave function is totally symmetric, thus in order for equation 13 to be non-zero and the vibrational mode infrared active, at least one of the Cartesian coordinates; x, y or z, must be contained in the appropriate representation. Raman activity requires that one of the components of the polarizability tensor be contained in the representation. This is seen in the character table as the squares and multiples of Cartesian coordinates or linear combinations there of, i.e.; x^2, y^2, xy, x^2-y^2, etc. A given vibrational mode may be infrared active and/or Raman active or neither. The knowledge of the symmetry of a molecule will allow the prediction of its spectrum, and the observed spectrum can either support or refute the proposed structure and symmetry of a molecule.[18] The importance of these considerations can be seen in Chapter 4, when using normal coordinate calculations to determine molecular parameters.

CHAPTER 3
THE INFRARED CHARACTERIZATION OF THE LINEAR ISOMERS OF C_2N_2

Introduction

The three conformers of C_2N_2 have been of interest to experimentalists and theorist alike. Cyanogen, NCCN, the most stable of these is easily prepared and purified, has been well-characterized experimentally.[20] The remaining isomers; isocyanogen, CNCN, and diisocyanogen, CNNC, are more difficult to synthesize and observe.

Stroh *et al.* report the matrix-isolation IR characterization of the products of the flash vacuum thermolysis of norbornadieone azine.[21] This precursor is a complex organic molecule and yields multiple products which include all three linear isomers of C_2N_2. Stroh and coworkers were able to characterize isocyanogen; but only a tentative assignment could be made for one stretching frequency of diisocyanogen, the least stable of the three conformers. Isocyanogen has been produced by pyrolysis of n-cyano-2,3-diphhenyl-cyclopropeneimine.[22] Additional investigations were done by Maier and co-workers using the microwave discharge of acetylene / nitrogen mixtures.[23] Both these strategies produce numerous organic byproducts.

We chose to produce these two transient species by the corona discharge[24] of cyanogen as shown in figure 3-1. This allows us to obtain a matrix without the extraneous products of the earlier thermolysis experiment. Isotopic labeling enabled the investigation of CNNC fundamental.

Experimental

Isocyanogen and diisocyanogen were produced by introducing a stream of 1% cyanogen in argon at right angles to a corona discharge[24] of pure argon gas. The argon used was 99.999% pure and obtained from Airco. Unlabeled cyanogen was obtained from Matheson at 98.5% purity. $N^{13}C^{13}CN$ and $^{15}NCC^{15}N$ were produced according to the synthesis described by Janz[25] starting with appropriately labeled KCN. This was obtained from Cambridge Isotope Laboratories each with 99% enrichment and 98+% purity. The discharge products were condensed onto a gold surface at 4K.

A schematic of the experimental setup can be seen in figure 3-2. Cooling for this system is done using an Oxford Continuous Flow Variable Temperature Insert. This liquid helium refrigeration system allows temperatures as low as 1.7K to be reached and maintained. The use of a heater assembly and helium flow rate control allows temperatures as high as room temperature to be obtained. The system is pumped to a vacuum on the order of 10^{-8} torr using a

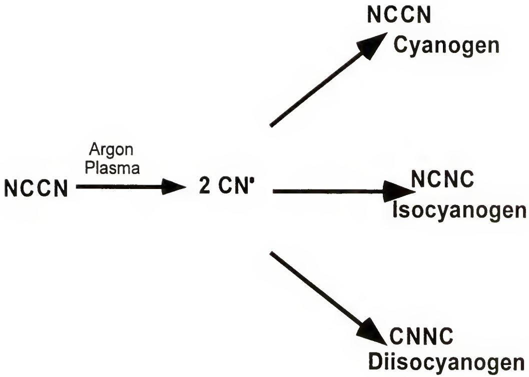

Figure 3-1 Production of CN dimers by corona discharge.

Varian V-450 molecular turbo pump. The deposition surface is a gold plated copper block, polished and dimensioned to allow the use of 8 separate sample positions between cleanings. The deposition surface is attached to a rotatable rod fitted with a hydraulic lift. This allows the matrix to be deposited in the lower chamber and then raised into position to obtain spectra. Absorption spectra were measured by reflection using a vacuum Fourier transform infrared spectrometer (Bruker IFS-133V). The mid-infrared region (400-4800cm^{-1}) was recorded at 1cm^{-1} resolution using a liquid nitrogen cooled mercury-cadmium-telluride (MCT) detector. The far-infrared region was investigated using both a DGTS-polyethylene detector with a 3.5 µm Mylar beam splitter (200-600cm^{-1}) and a silicon bolometer (370-20cm^{-1}).

The use of the corona discharge technique with matrix isolation has been described by Bai and Ault.[26] The development of this technique for use in our lab can be found in reference 27. Figure 3-3 shows a detailed schematic representation of the discharge tube. This discharge method results in the production of highly excited argon atoms, free electrons and vacuum ultraviolet radiation,[24] all of which may cause the dissociation of a precursor molecule.

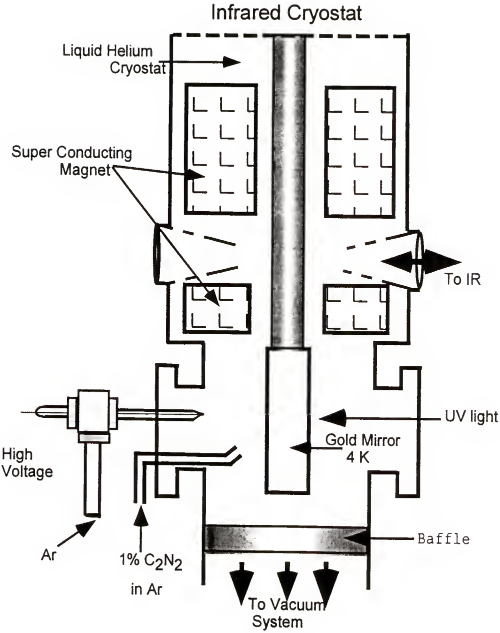

Figure 3-2 Cutaway side schematic of sample chamber.

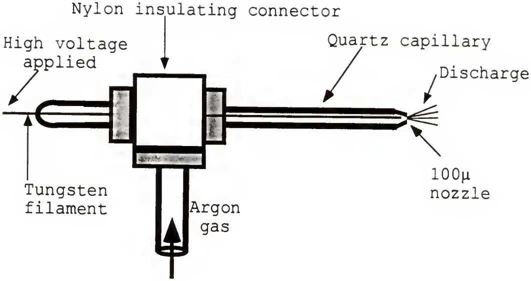

Figure 3-3 Corona discharge apparatus.

Results and Discussion

Figures 3-4 and 3-5 show the infrared spectra of the argon matrices containing the different isotopomers of C_2N_2. In addition to the three linear C_2N_2 isomers observed, CN radical and the trapped impurities of CO, CO_2 and water are seen. $^{13}CO_2$ was a by-product of the ^{13}C labeled cyanogen synthesis and is also visible in the appropriate spectrum. The fundamental bands for isocyanogen and diisocyanogen are indicated in the figures and summarized in table 3-1. Isocyanogen bands are denoted as ν_n, all the other peaks are labeled by species. The normal coordinate analysis of CNCN was performed using the PC version of ASYM20.[28] This procedure, as described in detail in Chapter 4, provided the predicted isotopic shifts in table 3-2 and also the force constants shown in table 3-3. Ab initio calculations on CNCN and CNNC were performed using Gaussian 94 at the MP2 level with a 6-31g* basis set.[29] The choice of this level of calculation and basis set was determined by comparing the published theoretical calculations to the experimental results known for cyanogen.[30-34] The simplest method shown to provide acceptable scaled calculated frequencies was then employed. The isotopic shifts calculated in this way are also given in tables 3-2 and 3-3.

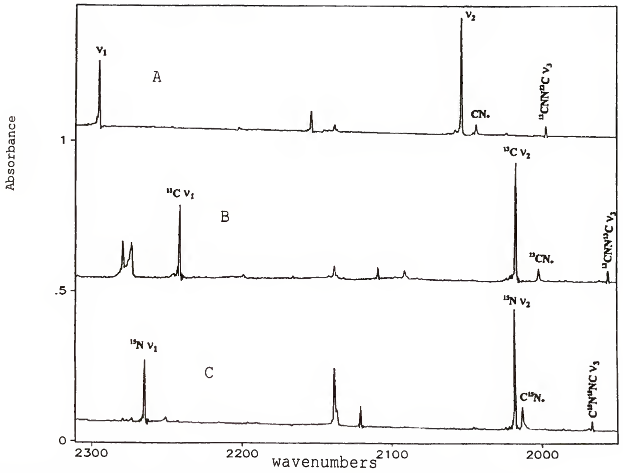

Figure 3-4 FTIR spectrum of C_2N_2 [(A) $^{12}C_2{}^{14}N_2$, (B) $^{13}C_2{}^{14}N_2$ and (C) $^{12}C_2{}^{15}N_2$] in argon deposited at 4K taken at $2 cm^{-1}$ resolution.

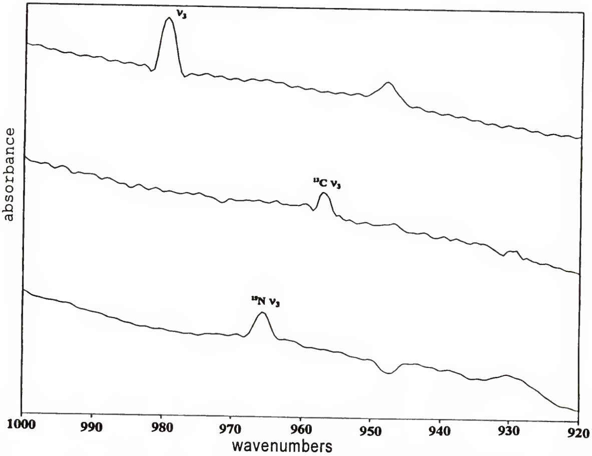

Figure 3-5 FTIR spectrum of C_2N_2 in argon.[(A) $^{12}C_2{}^{14}N_2$, (B) $^{13}C_2{}^{14}N_2$ and (C) $^{12}C_2{}^{15}N_2$ in argon at 4K.

Table 3-1 Observed fundamental band positions of isocyanogen and diisocyanogen in solid argon at 4K.

	$^{12}CN^{12}CN$ [a]	$^{12}CN^{12}CN$ [b]	$^{13}CN^{13}CN$ [a]	$C^{15}NC^{15}N$ [a]
ν_1	2294.0	2294.4	2241.5	2250.6
ν_2	979.7	979.2	956.6	965.7
ν_3	2053.9	2053.7	2001.85	2012.9
ν_4	466.1 / 467.7	468.5 / 467.2	457.0 / 456.1	462.4 / 463.3

	ν_3 Obs.
$^{12}CNN^{12}C$	1997.0
$^{13}CNN^{13}C$	1955.6
$C^{15}N^{15}NC$	1966.7

[a] This work

[b] Bands reported by Stroh *et al.*[21]

Table 3-2 Observed and calculated isotopic shifts for isocyanogen and diisocyanogen.

	Obs. $\Delta\nu$	Calc.$\Delta\nu$(norm)[a]	Calc. $\Delta\nu$(MP2)[b]
$^{12}C \rightarrow {}^{13}C$			
ν_1	-52.5	-49.9	-50.5
ν_2	-23.0	-18.1	-17.2
ν_3	-52.1	-45.0	-41.6
ν_4[a]	-12.0	-9.0	-12.0
$^{14}N \rightarrow {}^{15}N$			
ν_1	-43.4	-33.9	-33.1
ν_2	-14.0	-19.1	-17.8
ν_3	-41.0	-33.5	-33.0
ν_4[a]	-5.6	-6.0	-6.1

	ν_3 Obs.	$\Delta\nu_3$ Obs. [a]	$\Delta\nu_3$ Calc.[b]
$^{12}CNN^{12}C$	1997.0	---	
$^{13}CNN^{13}C$	1955.6	-41.4	-42.0
$C^{15}N^{15}NC$	1966.7	-30.3	-30.9

[a] Normal coordinate calculation as described in chapter 4.

[b] uncorrected *ab initio* calculation as described in text.

Table 3-3 Force constants for isocyanogen as calculated using normal coordinate analysis.

$C^aN^aC^bN^b$

	Force constant in aJ/Å^2 (mdyne/ Å)
Stretching	
$f(C^bN^b)$	17.5612
$f(C^aN^a)$	15.4077
$f(N^aC^b)$	8.8744
Bending	
$f(C^aN^a, N^aC^b)$	0.8533
$f(C^bN^b, N^aC^b)$	1.1971
$f(C^aN^a, C^bN^b)$	0.0302

The observed frequencies for unlabeled CNCN agree well with those reported by Stroh *et al.*,[21] for ν_1, ν_2, and ν_3. The ν_4 bend is difficult to see in our spectra but appears to fall at a lower wavenumber than reported in earlier work. Isotopic shifts support the new assignment of this band. In spite of an extensive effort to observe the ν_5 bend in the far infrared region, it was not possible to make an assignment for this mode.

Due to symmetry constraints, there is only one IR active fundamental for diisocyanogen. Stroh *et al.* tentatively assign a band at 1996.4 cm^{-1} as the ν_3 asymmetric stretch of CNNC. We observe a band at 1997.0 cm^{-1} for ^{12}CNN^{12}C, supporting their assignment. Isotopic substitution leads to the frequencies and shifts reported in table 3-2. The assignment of this band as CNNC is supported by comparison to the *ab initio* predicted shifts and also by the use of the Teller-Redlich product rule. The Teller-Redlich product rule states for isotopic molecules that the ratio of the frequencies, ω_i/ω, for all vibrations in a symmetry type is dependent on only the mass and geometry of the molecule.[28] Therefore isotopic substitution does not affect the molecular force field, and the assignment of isotopic shifts can be investigated without a complete set of vibrational frequencies. Fortunately the one IR active vibration of CNNC, ν_3, is the only fundamental mode of the symmetry type $\Sigma^+{}_g$.

The spectra shown in figure 3-4 provide the definite experimental observation of diisocyanogen, and provide agreement with work done by Maier *et al.*[28] This molecule is difficult to observe in part due to the low barrier to rearrangement. A noticeable decrease in the intensity of the observed ν_3 band was seen on annealing the argon matrix to 32K to allow increased mobility of the trapped species.

Further work on this system was done to attempt to obtain the FT-Raman spectrum. While unsuccessful, this would have allowed a normal coordinate treatment analogous to that performed on isocyanogen to be used to characterize the CNNC isomer. As a centro-symmetric molecule diisocyanogen obeys the rule of mutual exclusion; that is, modes are either infrared or Raman active but never both. Refer to Chapter 2 of this work for more information regarding the selection rules for infrared and Raman spectroscopy.

CHAPTER 4
NORMAL COORDINATE ANALYSIS

A normal mode is a discrete, synchronous motion of atoms within a molecule which can be individually excited.[35] Normal modes can be approximated as harmonic oscillators. This allows the calculation of frequencies for given vibrations. The choice of a coordinate system for the molecule can greatly simplify this task. In addition to standard Cartesian coordinates, a molecule can be described in internal, normal or symmetry coordinates. The choice of a coordinate system is based primarily on the symmetry of the molecule.

The goal of a normal coordinate analysis will be to relate the frequency of a vibrational mode to the structure of the molecule; the internal forces present; and to the masses and displacements of the atoms involved.[36] All nonlinear molecules have 3N-6 degrees of vibrational freedom, with linear molecules allowed 3N-5. The vibrational frequencies are accessible through solving the secular equation comprising the potential energy matrix. If this is done in Cartesian space then a 3N x 3N determinant must be solved.[36] This results in many more force constants than frequencies and no exact solution can be determined.

The problem becomes more meaningful when moved to an internal coordinate system. Expressing a vibration in terms of displacement from equilibrium positions reduces the order of the matrix to 3N-6 x 3N-6 (or to 3N-5 x 3N-5 for linear systems). These linear combinations of the Cartesian coordinates fall into five types: bond stretches, torsions; angle, linear angle and out-of-plane bends.[27] The internal coordinates yield force constants that are linked to the movement of specific atom groups and thus directly describe the structure of the molecule.

Further simplification can be accomplished by combining internal coordinates to form symmetry coordinates. Each vibration will be expressed as a linear combination of internal coordinates. Equivalent coordinates are combined to give sets that transform according to the point group of the molecule. All symmetry coordinates must be normalized and form an orthonormal set.

It is possible to set up and solve a secular equation given by using Newton's second law (force = mass x acceleration), but in practice it is more convenient to combine the potential and kinetic energy terms using the law of conservation of energy.[20] E.B. Wilson used this second strategy in developing his classic FG Matrix method.[16]

The FG matrix method involves setting up a force constant matrix, F, which describes the potential energies of the molecule, and a geometry or G matrix, which is a modified description of the kinetic energy.[37] The method assumes that all vibrations are small amplitude harmonic oscillations. The F matrix is a N x N matrix containing the primary and interaction force constants. The G matrix is more complicated to develop. Wilson defines the G matrix elements in terms of symmetry coordinates as

$$G_{lj} = \sum_p \mu_p g_p S_j^{(t)} \bullet S_l^{(t)} \qquad (1)$$

where p tells which atom t, or equivalent set is being considered, μ_p is the reciprocal mass of atom t, g_p tells how many atoms set p contains.[7] The S vectors are found by

$$S_j^{(t)} = \sum_k U_{jk} S_{kt} \qquad (2)$$

where j tells which symmetry coordinate is being considered, U_{jk} is the coefficient of the k^th internal coordinate, and S_{kt} is expressed from unit vectors along chemical bonds to describe displacement from equilibrium.[38]

The calculation of G matrix elements can be time consuming; fortunately there are a finite number of symmetry species that allowed the compilation of tables to provide G matrix elements. Once the symmetry of the molecule has been established, G_{jl} elements can be found in appendix VI of Wilson, Decius and Cross for nonlinear molecules[18] and in reference 39 for linear molecules.

Combining the **F** and **G** matrices as

$$\left|\mathbf{F}-\mathbf{G}^{-1}\lambda\right|=0 \qquad (3)$$

allows the calculation of either λ from force constants or force constants from known frequencies. The following example details setting up the **FG** matrix treatment of cyanogen.

Cyanogen, NCCN, is a linear molecule possessing 3N-5 or 7 degrees of vibrational freedom. This molecule is of $D_{\infty}h$ symmetry, giving two stretches of σ_g symmetry and one of σ_u symmetry. There are also two doubly degenerate bends one of π_g and one of π_u symmetry, as shown in figure 4-1b. To begin, 3N-5 internal coordinates must be assigned. These will be assigned as from figure 4-1a.

Three will represent changes in bond length, Δr_{12}, Δr_{23} and Δr_{34}. Four will correspond to bond angle changes, θ_{1x}, θ_{1y}, θ_{2x} and θ_{2y}. Since this is a symmetric molecule, it will simplify matters to reduce the internal coordinates to symmetry coordinates. To do this, equivalent internal coordinates will be combined according to the $D_{\infty}h$ point

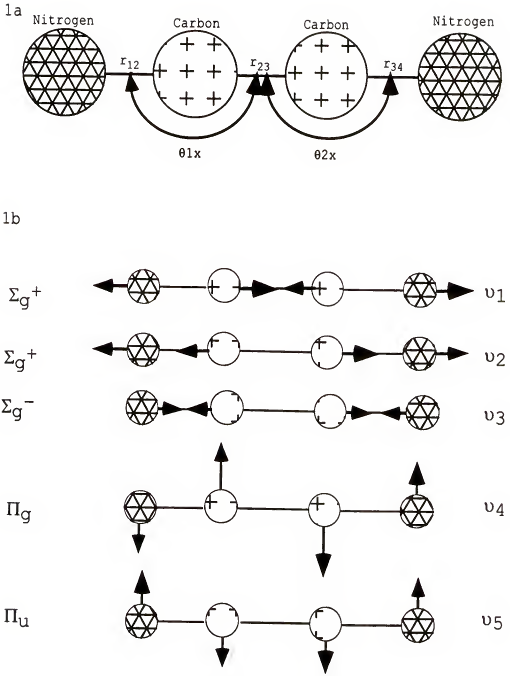

Figure 4-1. Normal modes of cyanogen.
a) Assignment of variables
b) Symmetry and motion of individual modes.

group, normalized and shown orthonormal. Figure 4-1b shows that the Δr_{12} and the Δr_{34} coordinates are equivalent upon inversion of the molecule. If we take linear combinations of these two coordinates we get

$$\mathfrak{R}_1=(2)^{-1/2}(\Delta\ r_{12}+\Delta\ r_{34}) \tag{4}$$

and

$$\mathfrak{R}_2=(2)^{-1/2}(\Delta\ r_{12}-\Delta\ r_{34}) \tag{5}$$

Checking the character table for $D_{\infty}h$, we see that $\mathfrak{R}_1$ transforms as σ_g and $\mathfrak{R}_2$ transforms as σ_u. Symmetry coordinates are normal if they meet the criterion that

$$\Sigma_k(U_{jk})^2=1 \tag{6}$$

and sets of equations are orthogonal if they fit the requirement that

$$\Sigma_k U_{jk} U_{1k}=0 \tag{7}$$

$\mathfrak{R}_1$ and $\mathfrak{R}_2$ can be shown to satisfy these parameters.

The remaining symmetry coordinates are established in the same way yielding:

$$\mathfrak{R}_3=\Delta\ r_{23} \qquad \sigma_g \tag{8}$$

$$\mathfrak{R}_4=(1/2)(\ \theta_{1x}-\theta_{1y}+\ \theta_{2x}-\ \theta_{2y}) \qquad \pi_g \tag{9}$$

$$\mathfrak{R}_5=(1/2)(\ \theta_{1x}+\theta_{1y}+\ \theta_{2x}+\ \theta_{2y}) \qquad \pi_u \tag{10}$$

The next step is to establish a **G** matrix. Since we are dealing with a linear molecule, we will obtain these elements from reference 39. Matching the cyanogen vibrations to the elements given yields:

$$G_{11}=\mu_N+\mu_C \tag{11}$$

$$G_{22}=2\mu_C \tag{12}$$

$$G_{12}=-\mu_C \tag{13}$$

$$G_{33}=\mu_C+\mu_N \tag{14}$$

$$G_{44}=G_{55}=\rho^2_{12}\mu_N+\rho^2_{23}\mu_C+\mu_C(\rho^2_{12}+\rho^2_{12}+2/3\rho^2_{12}\rho^2_{12}\cos 180) \tag{15}$$

where μ_x is the reciprocal mass of atom x.

Now just the stretches will be considered and the **f** matrix will be established as shown in table 4-1. This matrix is labeled **f** because it has not yet been symmetrized. This will be done by taking

$$\mathbf{F}=\mathbf{U}\mathbf{f}\mathbf{U}^{-1} \tag*{[16]}$$

where **U** is the matrix of the normalization coefficients for each internal coordinate found in the appropriate symmetry coordinates. A **U** matrix must be found for each symmetry group of vibrations. $\mathbf{U}^{-1}$ is the inverse of **U**, since U is orthogonal, $\mathbf{U}^{-1} = \mathbf{U}^t$, simplifying the calculation. Table 2 shows the **U** matrix for the σ_g stretches. Now **F** and **G** can be combined as shown in equation 3. The use of symmetry coordinates causes this to be a block-diagonal matrix. The secular determinate for cyanogen will be separable into one

Table 4-1. The **f** matrix elements for cyanogen stretches.

	Δr_{12}	Δr_{23}	Δr_{34}
Δr_{12}	f_{CN}	$f_{CN\ CC}$	f_{cncn}
Δr_{23}	$f_{CN\ CC}$	f_{CC}	$f_{CC\ CN}$
Δr_{34}	$f_{CN\ CN}$	$f_{CC\ CH}$	f_{CN}

Table 4-2 **U** matrix elements for σ_g vibrations.

σ_g	Δr_{12}	Δr_{23}	Δr_{34}
$\Re_1$	$(2)^{-1/2}$	0	$(2)^{-1/2}$
$\Re_3$	0	1	0

2 x 2 matrix arising from the two σ_g vibrations, and 1 X 1 matrices resulting from the σ_u, π_g and π_u vibrations. While it is possible to solve this problem by hand larger and/or less symmetric molecules result in higher order secular equations making it desirable to create a computer program able to handle such problems with greater speed. There are several programs available to accomplish this.

One such program available as a part of the Quantum Chemistry Program Exchange is QCMP012 General Vibrational Analysis Programs using the Wilson GF Matrix Method for a Generalized Unsymmetrized Molecule. This was written by Douglas F. McIntosh and Michael R. Peterson, and converted to run on PC equipment by Timothy J. O'Leary. QCMP012 uses three programs to arrive at a solution to the general vibrational equation. It is not necessary to use symmetry coordinates, but it requires that new input files be created after each step. While the program should be capable of computing linear angle bends such as the ν_4 and ν_5 modes of cyanogen, this could not be accomplished in our lab.

Another program available to handle this type of calculation is ASYM20 written by Lisa Hedberg and Ian M. Mills. A detailed description of this program can be found in reference 27. Also available through the Quantum Chemistry Program Exchange, this program provides a procedure allowing the calculation of harmonic frequencies and force constants requiring only one input file. The program also has provisions allowing it to handle degeneracies, but it requires the use of symmetrized force constants in these cases. While Cartesian coordinates are used initially the **U** matrix is required by the program to allow it to develop symmetry blocking, when a refinement of force constants is requested. The program has in addition to simple vibrational equation capabilities, parameters allowing for calculation of rotational and thermodynamic properties.[27] This is the program that was used in this work to calculate vibrational frequencies and force constants for cyanogen, isocyanogen and diisocyanogen.

In order to perform a complete normal coordinate analysis, it is necessary to have as many frequencies corresponding to normal modes of the molecule as force constants to determine. In order to fulfill this requirement for cyanogen and isocyanogen, isotopic substitution was used. By using the frequencies of the infrared active fundamentals for three different isotopomers of each molecule, the force constants corresponding to the stretching modes of these species can be determined using the ASYM20PC program. These results have been presented in table 3-3.

CHAPTER 5
DIDEHYDROGENATED DERIVATIVES OF POLYCYCLIC AROMATIC HYDROCARBONS

Introduction

Polycyclic aromatic hydrocarbons or PAHs are of interest as environmental pollutants, and of particular relevance here, as astrophysical molecules. These species have been proposed as the source of several infrared emission features seen radiating from celestial objects and in the interstellar medium.[40-42] It has been proposed that the larger PAH systems may be likely candidates for the bands seen at 3050, 1615, 1310, 1150, and 885cm^{-1}.[43] Originally, it was suggested that these molecules might be trapped inside dust grains.[43] Later theories proposed that these molecules were free, isolated species.[41,44] The neutral species were investigated in the laboratory and the relative intensities, as well as band shapes and positions of the observed infrared bands did not provide an encouraging match to the astrophysical spectrum.[45]

The environment faced by molecules in these regions is rich in ultraviolet radiation. In such a harsh setting, it is unlikely that the molecule would be found in its neutral, unperturbed state. One model that has been proposed is that these species might exist in an ionized form. The cations of several of these PAH molecules have been investigated by Vala and co-workers,[46-48] as well as by the Allamandolla group.[49] The ionized species are seen to give better agreement with respect to the relative intensities of the observed interstellar features than the neutrals, however frequency and band shape discrepancies within the overall spectrum remain.[42]

In the case of free or isolated PAH molecules, it is reasonable to also propose that they contain some degree of dehydrogenation. It has been difficult to test this theory due to the lack of laboratory infrared spectra of dehydrogenated PAH molecules. The simplest aromatic system is a benzene molecule, which then yields the di-dehydrogenated derivative known as benzyne. This is shown in equation 1.

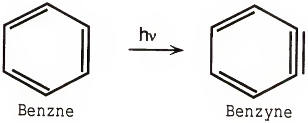

(1)

This molecule was initially isolated and characterized through its infrared spectrum by Chapman and colleagues.[50]

Through the prolonged photolysis of phthalic anhydride it is possible to create ortho-benzyne.[50-54] This molecule was shown to possess significant triple bond character, and has been the subject of intense experimental and theoretical scrutiny. It is well characterized structurally. A normal coordinate treatment performed by Nam and Leroy has provided a vibrational force field that provides excellent agreement with experimental data.[54,55]

Benzyne has been well studied both experimentally and theoretically, however very little work has been done on the larger PAH analogues of this system. While there has been limited gas phase ultraviolet work done on the naphthalene and anthracene congeners of benzyne, no infrared spectra of these systems has been thus far available. It is only recently that theoretical calculations regarding the infrared frequencies and intensities of these molecules have become available.[45,56] The work done on naphthyne derivatives by Pauzat, Talbi, and Ellinger[56] (PTE) encouraged the publication of the matrix isolation infrared spectrum of 2,3-naphthyne to be described in this work.[57]

Experimental

2,3-naphthyne was produced through the photolysis of matrix isolated 2,3-naphthalene anhydride. This precursor molecule was synthesized in our lab following the procedure of Campbell and Grimmett.[58] The reaction of phenylpropiolic acid with propiolic acid was carried out in a solution of acetic anhydride according to the reaction:

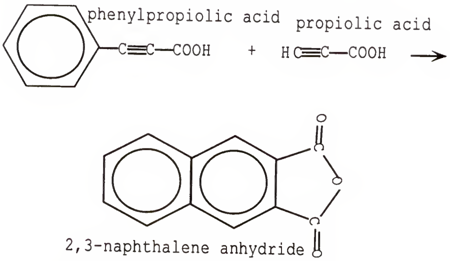

(2)

The starting mixture was heated to 70°C for 2 hours followed by further heating to 100°C for 5 hours. This yielded a deep brown solution. After cooling to room temperature, the solution was added to distilled water to give a pale brown precipitate. The precipitate was removed and treated with 3 molar NaOH. While not all the precipitate could be dissolved, an orange-brown solution containing 2,3-

naphthalenedicarboxylic acid was formed. The solution was decanted off and concentrated HCl was added drop wise to precipitate the anhydride. This pale white precipitate was then filtered and dried before recrystallization from glacial acetic acid. Further purification was accomplished through vacuum sublimation. Initially the sample was heated to 90^0C to drive off any remaining acetic acid, and then the 2,3-naphalene anhydride was sublimed at 170^0C under the vacuum generated by a water aspirator. The melting point of the resulting material was found to be 225-231^0C as compared to the value of 246^0C cited by Campbell and Grimmett.[58] To insure that the product obtained was 2,3-naphthalene anhydride, mass spectrometry was used. These spectra supported the identity of the material and indicated that the product was relatively pure.

The 2,3-naphthalene anhydride was then vacuum sublimed at 90^0C and co-condensed with neon (Matheson, 99.999%), argon (Airco, 99.999%), or Krypton (Airco, 99.999%) onto a gold surface at 4K. The arrangement of the sample deposition chamber of the infrared spectrometer is shown in figure 5-1. The apparatus shown is described in detail in Chapter 3 of this thesis. Deposition occurs at a rate of approximately 8-12 mmoles per hour. The resulting matrix

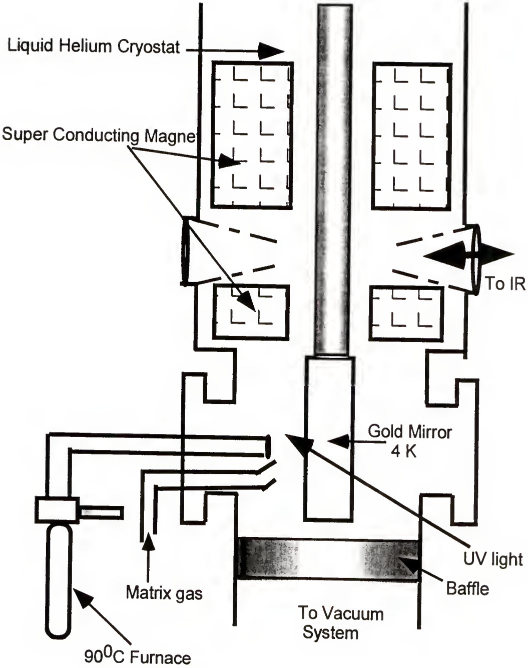

Figure 5-1 Cross-section of sample chamber and cryostat.

is estimated to be 1:500 molecules of anhydride to noble gas. These depositions were carried out over a period of three hours, after which the infrared spectrum of the precursor molecule was obtained. The sample was then irradiated using an AH-6 water-cooled high-pressure mercury lamp. The photolysis was carried out over a period of three hours, during which the temperature of the matrix was held at 10-12K. Intermittent monitoring of the matrix indicated that no further reaction occurred after approximately 2 hours. The infrared spectrum of the matrix after photolysis was obtained and the difference spectrum comparing it to the original matrix was calculated. Measurements were taken in both the mid and far infrared regions.

The analogous experiment was performed on the 1,2-naphthalene anhydride molecule. This precursor was obtained from TCI America, and was vacuum sublimed to provide further purification. The experimental procedure is identical to that described above, except that the sublimation temperature used was slightly higher at 100^0C. This molecule, as well as the 2,3 derivative, was also isolated in a doped argon matrix containing natural and carbon 13 labeled carbon monoxide at varying concentrations.

An alternate route for the production of di-dehydrogenated molecules was attempted by using di-iodide molecules as precursors. In these experiments ortho di-iodobenzene (Eastman, 99%) was sublimed at room temperature into an argon matrix. The apparatus was set up as shown in figure 5-1, except that it was necessary to include a stopcock above the di-iodobenzene to prevent unwanted sublimation. The successful photolysis of this system required the use of elevated temperatures (20-30K) and a low-pressure xenon lamp.

2,3-Naphthyne

The bands projected down in figures 5-2, 5-3 and 5-4 show the infrared spectrum of 2,3-naphthalene anhydride (2,3-NA) in neon and argon matrices. The upwardly projected bands belong to the difference spectrum arising after photolysis. Irradiation of 2,3-NA produced equimolar amounts of naphthyne, CO, and CO_2 according to the reaction

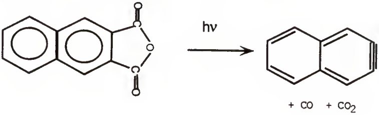

(3)

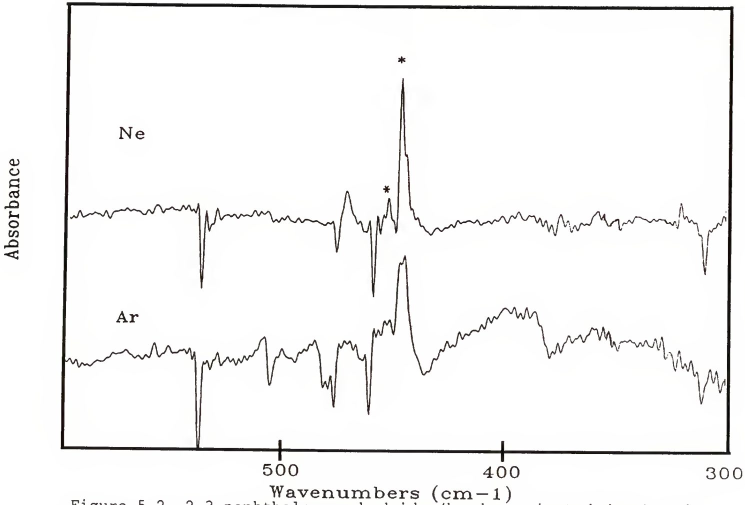

Figure 5-2 2,3-naphthalene anhydride (bands projected down) and 2,3-naphthyne (*bands) in solid argon and neon.

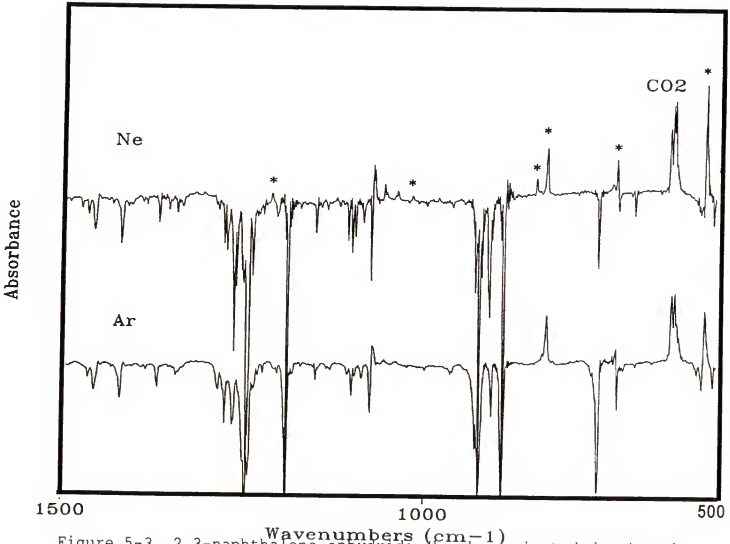

Figure 5-3 2,3-naphthalene anhydride (bands projected down) and 2,3-naphthyne(*bands) in solid argon and neon.

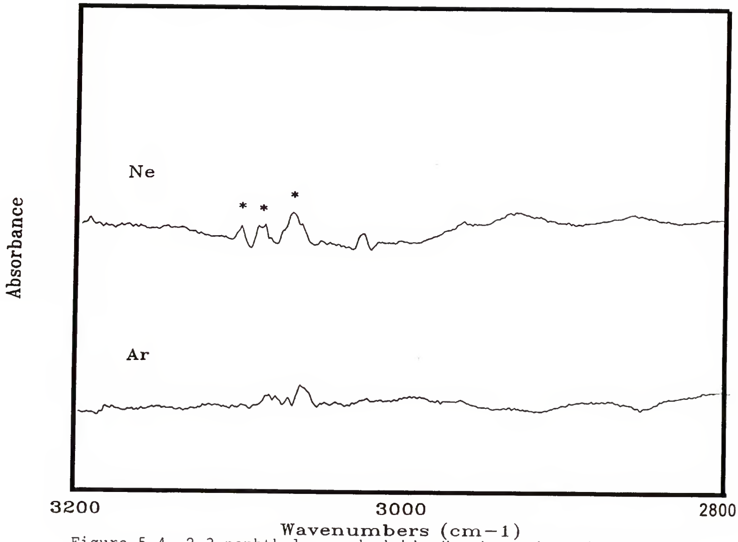

Figure 5-4 2,3-naphthalene anhydride (bands projected down) and 2,3-naphthyne (*bands) in solid argon and neon.

The flash photolysis of naphthalene anhydrides has been used by Lohmann[59] to obtain the ultraviolet spectrum of didehydrogenated naphthalenes. A similar method has been used to produce and characterize benzyne from phthalic anhydride.[50-59] The starred bands in the neon spectra are attributed to 2,3-naphthyne and are listed in table 5-1. Also included in this table are the corresponding band positions as seen in argon and krypton matrices. These assignments were made through the comparison of frequencies and relative intensities to the theoretical infrared spectrum calculated by PTE. The calculated bands and corresponding intensities are also shown in table 5-1. Only those bands predicted to have an intensity of at least 10km/mol were considered.

The relative intensities of the observed naphthyne bands were calculated for the spectrum taken in a neon matrix. This was accomplished by taking the most intense observed spectral feature for 2,3-naphthyne and setting the observed intensity equal to its theoretical counterpart. This band is calculated to lie at 438cm^{-1} with a predicted intensity of 92km/mol, and is assigned in the neon matrix at 445.5cm^{-1}. This C-C-C bending mode is both calculated and observed to be the most intense band in the 2,3-

Table 5-1 Observed fundamental band positions and intensities of 2,3-naphthyne in solid neon, argon and krypton as compared to predicted values.

Assignment[a]	2,3obs Ar	2,3obs Kr	2,3obs Ne	rel int[b]	2,3 calc[c]	Calc int[c]
r(CH)	3082		3098	8	3090	13
r(CH)	3078		3084	10	3078	19
r(CH)	3063		3069	16	3065	21
β(CH)/R(CC)			1213.1	4	1232	23
R(CC)/β(CH)			1018.3	2	1010	17
α(CCC)		847.6	848.6	9	869	24
ε(CH)	833	832.2	834.1	37	843	74
τ(CCC)	738	736.7	738.6	47	739	51
α(CCC)	618	616.2	618.1	79	600	54
τ(CCC)			451.8	9	446	22
α(CCC)	444	444	446.5	92	438	92

[a] r(CH),C-H stretching vibration; R(CC),C-C aromatic vibration; β(CH),C-H in-plane bending vibration; α(CCC), C-C-C bending vibration; ε(CH),C-H out-of-plane bending vibration; τ(CCC), C-C-C out-of-plane bending vibration

[b] for neon matrix as described in text.

[c] from reference 56.

naphthyne spectrum. The relative intensities of the remaining observed bands were assigned by comparing their integrated peak areas to the area of the 445.5cm^{-1} band. These peaks show reasonable agreement with the calculated intensities given in table 5-1. In general computed intensities of infrared absorption bands are not considered to be completely reliable, and can easily be in error by a factor of 2.[50-62] It should also be considered that the theoretical assignments of ortho-benzyne have been a topic of controversy and revision in recent years.[60,63-65] This will be discussed later in this work. As would be expected, there are strong bands assignable to CO and CO_2 seen in the spectra after photolysis of the precursor matrix.

The experiment was repeated using three different matrix gases. As would be expected, the neon spectrum provided the sharpest observed spectrum. While there is in general very good agreement between the spectrum in neon and argon matrices, there are some differences. There is a relatively strong band observed at 471.1cm^{-1} in the neon matrix, which has no argon matrix counterpart. Since there are two strong background absorbances in this neighborhood, it is likely that this feature is an artifact. There are two bands at 834.1 and 848.6cm^{-1} in neon, which may be seen as overlapping at 833cm^{-1} in argon. The assignment of the band corresponding to the calculated 1010cm^{-1} feature according to PTE was difficult. In the neon spectrum, there are five progressively weaker features observed at 1072.3, 1054.0, 1037.6 1018.3 and 981.6cm^{-1}. The four strongest features appear slightly shifted in the argon matrix as well. The assignment of the 1018.3cm^{-1} band to the 2-3 naphthyne molecule as shown in table 5-1 is made rather arbitrarily based on its proximity to the calculated frequency. PTE calculate the most intense feature of naphthyne cation to lie at 1093cm^{-1} and for additional bands to be seen at 1034 and 1028cm^{-1}. It is possible that some of the bands observed in this region of the spectrum could result from the ionized form of naphthyne.

1,2-Naphthyne

Figure 5-5 shows the spectrum of 1,2-naphthalene anhydride in neon with the bands projected down. The upwardly projected bands show the result of the difference spectrum obtained after photolysis. This reaction proceeds as shown in equation 4.

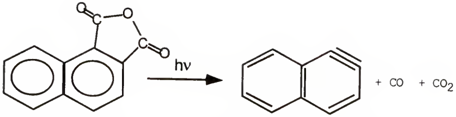

(4)

The bands shown in table 5-2 were assigned to 1,2-naphthyne in the same manner as described for the 2,3-naphthyne analog. This molecule was investigated in both neon and argon matrices, the assignments for the argon matrix spectrum are included in table 5-2. Relative intensities for the assigned bands were calculated as described above, and are included for both the neon and argon spectra. The observed agreement between theory and experiment was seen to be again reasonable, but the resulting spectra were not as clear as their 2,3-naphthyne counterparts, leading to more tenuous assignments for these bands. The clear evidence of CO and CO_2 being produced as a result of photolysis supports that 1,2-naphthyne was produced.

One factor in this experiment is that the naphthyne triple bond is very reactive toward complexation with the CO produced during the photolysis. This is seen when looking at the CO stretching region as shown in figure 5-6. The benzyne-CO complex has been studied by Hobza et al.[66] They used *ab initio* methods to investigate the relative

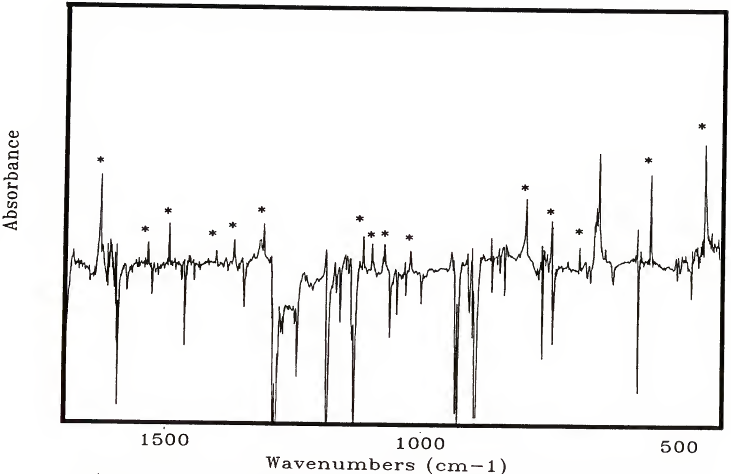

Figure 5-5 1,2-naphthalene anhydride (bands projected down) and 1,2-naphthyne(*bands) in solid neon.

Table 5-2 Observed fundamental band positions and intensities of 1,2-naphthyne in solid argon and neon as compares to predicted values.

assignment	*1,2obs Ar*	*rel. int.*		*1,2 obs Ne*	*rel. int*	*1,2 calc*	*1,2 calc int*
r(CH)		scaled to *peak				3086	13
r(CH)				scaled to *peak		3074	16
r(CH)						3065	9
R(CC)/β(CH)							
R(CC)/β(CH)				1537.1	12	1529	12
R(CC)/β(CH)				1496.6	19	1499	14
β(CH)/R(CC)	1365.4	56	51	1312.4	15	1295	15
				1115.7	17		
R(CC)/β(CH)				1098.3	11	1103	7
				1073.2	13		
R(CC)/β(CH)	1093.9	16	14	1024	16	1014	8
α(CCC)						838	6
ε(CH)	798	82	74*	800.4	36	788	73
τ(CCC)	748.1/ 757.1	68/63	62/57	750.2		737	62
α(CCC)	557.1	60	54	558.3	60	543	24
τ(CCC)						438	5
α(CCC)	452.3	96*	87	454.2	96*	426	96

stability of van der Waal's complexes with different orientations of CO with respect to the benzyne triple bond. Their work investigates 6 possible geometric isomers of the complex, two sandwich structures and four planar complexes. The sandwich structures are found to be most stable. However, 5 of the 6 possible orientations are predicted to be favored over the free molecules, and the difference in stability is on the order of 0.5kcal/mol. With this small difference in energy it is likely that a mixture orientations will be observed. Figure 5-6 shows a broad band that can be assigned the CO stretching mode of the 1,2-naphthyne complex in a neon matrix. It is reasonable to propose that band arises in part from overlap of two or more orientations of the CO moiety relative to naphthyne within the matrix.

The corresponding spectral feature of the CO-benzyne complex has been reported to show a variation of band shape upon warming of the matrix.[66] Figure 5-7 shows the CO stretching region of the 1,2-naphthyne in argon spectrum before and after annealing for 15 minutes at 32K. There is a very slight change in the relative intensities of the observed features. While this may indicate a relaxation toward a preferred orientation, there were no further

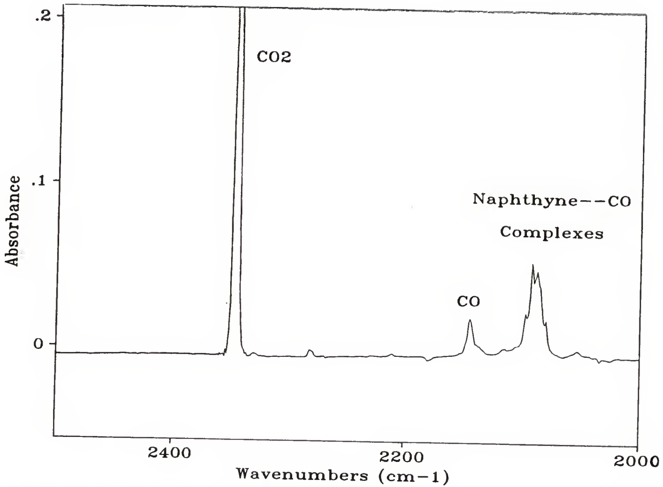

Figure 5-6 The FTIR spectrum of the CO stretching region of a neon matrix containing CO and 1,2-naphthyne.

changes observed at longer annealing times. It might be suggested that the changes observed are simply the relaxation of strain within the matrix, and that the barrier to rearrangement is too large to allow appreciable change to occur. The broad nature of the argon matrix lines makes it difficult to resolve any additional structure with this feature. Unfortunately, it was not possible to anneal the corresponding neon matrix.

It was hoped that by producing the naphthyne molecule in a matrix doped with additional CO further information could be gathered. The photolysis experiment was performed in CO/argon mixture matrices with concentrations ranging from 0.02-0.1%. The series of experiments resulted in a broad featureless absorption at the position of the complex CO stretching band. No further information was obtainable from these experiments. The close proximity of the CO molecule produced by the reaction makes it the preferred candidate for complex formation, thus ^{13}CO experiments were likewise unproductive.

Comparison of the 2,3 and 1,2 -Naphthyne Molecules

It is of particular interest to compare the band positions of the two isomers of naphthyne. These molecules differ only by the placement of the triple bond. Table 5-3

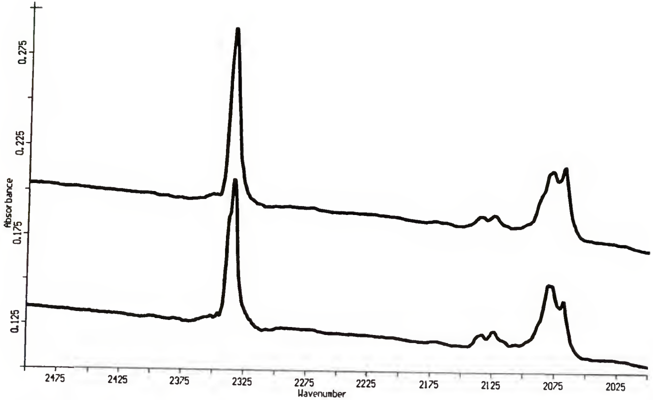

Figure 5-7 The Co stretching regin of an argon matrix containing CO and 1,2 -naphthyne. A) Original deposition at 4K. B) After annealing to 32K.

Table 5-3 Comparison of 1,2-naphthyne to 2,3-napthyne band positions as observed in solid neon.

assignment	*1,2 obs neon*	*2,3 obs neon*
r(CH)		3098
r(CH)		3084
r(CH)		3069
R(CC)/β(CH)		
R(CC)/β(CH)	1537.1	
R(CC)/β(CH)	1496.6	
β(CH)/R(CC)	1312.4	1213.1
	1115.7	
R(CC)/β(CH)	1098.3	
	1073.2	
R(CC)/β(CH)	1024	1018.3
α(CCC)		848.6
ε(CH)	800.4	834.1
τ(CCC)	750.2	738.6
α(CCC)	558.3	618.1
τ(CCC)		451.8
α(CCC)	454.2	446.5

shows a comparison of the observed and calculated[56] band positions for the two molecules. The observed bands in table 5-3 are reported for the molecules isolated in a neon matrix, the frequencies observed in argon and krypton can be seen in tables 5-1 and 5-2.

As expected, table 5-3 shows that the frequencies observed for the two molecules are different, but show similar general structure. One important difference in the two molecules is the relative arrangement of the remaining hydrogen atoms. Figure 5-8 shows a detailed diagram of each of the isomers. Note the appearance of what PTE refer to as solo and duo H atoms. This results in the predicted emergence of a band at 788cm^{-1} for the out-of-plane motion of the duo hydrogens of 1,2-naphthyne. This band is observed at 800.4cm^{-1} in neon. The solo hydrogens of 2,3-naphthyne give an observed neon matrix band at 834.1cm^{-1}, relative to the calculated value of 843cm^{-1}.[56]

In neither molecule was the C-C triple bond stretch, calculated to lie between 1920 and 2060cm^{-1}, observed. This is not unexpected as the calculated infrared intensity of this mode is very small, 1km/mol for the 1,2-naphthyne molecule, or 3km/mol for the 2,3 substituted structure. This band is predicted at 2059cm^{-1} for the 1,2 isomer, thus

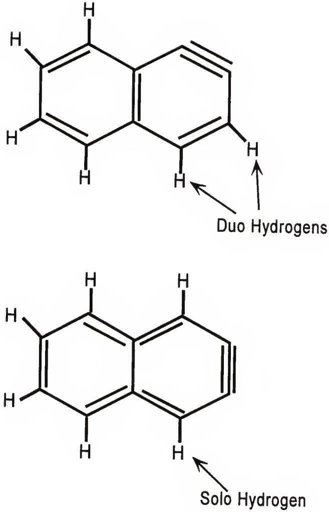

Figure 5-8 Naphthyne isomers showing the relative positions of the remaining hydrogen atoms.

it would likely be obscured by the presence of the CO stretching band of the complex as shown in figure 5-6. The 2,3 triple-bond stretch would be expected to be near 1950cm^{-1}, away from the CO stretching region. There is no band observed in this region. The assignment of the corresponding band for benzyne has been the subject of considerable controversy and revision.[64,67,68] The band at 2085cm^{-1} originally assigned to benzyne in an argon matrix has since been attributed to the ketene stretch of cyclopentadienylideneketene. This molecule has been shown to coexist in matrices with benzyne produced in the presence of CO.[64] It is the subject of heated debate as to whether this molecule is an intermediate in the formation of benzyne or if it is produced through the reaction of CO with benzyne.[69-71]

In an attempt to eliminate the interference caused by the presence of CO in the matrix, an attempt was made to synthesize the naphthyne derivatives from an alternate precursor. The formation of benzyne from dichlorobenzene has been demonstrated through collision-induced dissociation by Wenthold and colleagues.[72] In order to facilitate photochemical elimination the iodine derivatives of the appropriate aromatic hydrocarbons were used in our lab. Benzyne was successfully produced according to the reaction shown in equation 5. The identity of this product was easily confirmed through comparison with known spectra.

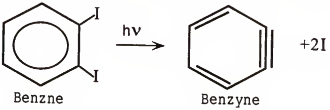

(5)

The analogous experiment for the appropriate di-iodonaphthalene molecules was hampered by difficulty in obtaining the starting products. After several failed synthesis attempts, a small sample of mixed isomers was obtained from Eastman Chemical. The inability to completely separate the different precursor molecules resulted in spectra that could not be reliably assigned to individual naphthyne isomers. The appearance of the spectra was encouraging, and this experiment should be pursued if a source of pure starting material becomes available.

Photolysis of 1,2,4,5 Benzenetetracarboxylic Dianhydride

It has been proposed that the doubly-didehydrogenated forms of PAH molecules would give a better match to observed interstellar spectra.[56] The simplest doubly-didehydrogenated molecule would be tetradehydrobenzene or benzdiyne. It might be expected that this molecule could be produced in the same manner as benzyne, starting instead from the dianhydride derivative of benzene as shown in equation 6.

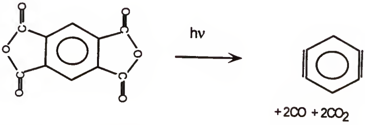

(6

This has been attempted by Moriyama and coworkers using two different photolysis schemes.[73] In each case, benzdiyne could not be isolated, with the observation of ring opening by-products seen instead. They propose that the failure to isolate this molecule could be due to the ease at which hydrogen migration might occur. They support this theory by successfully isolating the benzdiyne derivative of 1,4-bis(trifluoromethyl)-2,3,5,6-benzenetetracarboxylic dianhydride.[74] The addition of these highly electronegative substituents for the hydrogen atoms stabilized the strained ring. Since their original experiments were attempted only in an argon matrix at 12K, it was thought that the use of lower temperatures and alternate matrix environments might allow the observation of un-substituted benzdiyne. To this end, the reaction as shown in equation 6 was performed as described earlier in argon, neon and krypton matrices. The results of photolysis at 4K and 12 K were compared as well as the effects of different matrix gasses.

Figure 5-9 shows the spectrum of BDA in argon before (A) and after photolysis (B) at 4K, and following annealing the matrix to 32K (C). The disappearance of the band at 1811 cm^{-1} and the emergence of the 1793 cm^{-1} band is in agreement with the results presented in reference 73. They attribute the new band to the anhydride derivative of benzyne. This is species 1 as shown in figure 5-10. It is troubling that there is a band at this frequency in the spectrum taken before photolysis. This is apparent in the spectra of the precursor molecule in all the experiments performed in our lab, and seems also to be present in the spectrum shown in reference 73. They support their assignment of this peak species 1 through GC-MS analysis of a furan adduct produced through the photolysis of BDA in a doped argon matrix.

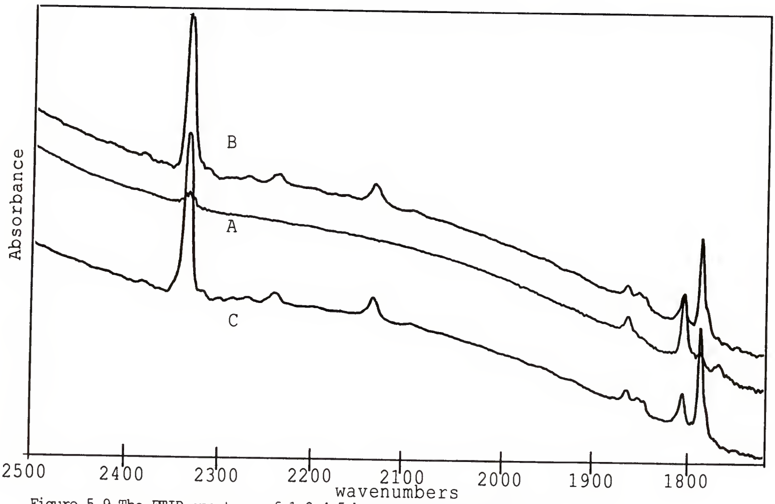

Figure 5-9 The FTIR spectrum of 1,2,4,5-benzenetetracarboxylic dianhydride in solid argon. A)Original sample. B)After photolysis C)Following annealing to 32K.

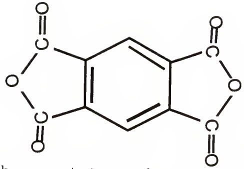

1,2,4,5-benzenetetracarboxlic dianhydride

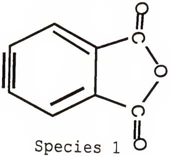

Species 1

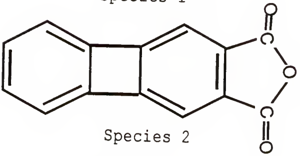

Species 2

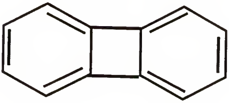

Species 3

Figure 5-10 Structures of proposed photolysis products of 1,2,4,5-benzenetetracarboxlyc dianhydride.

An alternate proposal for the carrier of this band would be to assign it to species 2 in figure 5-10. Biphenylene, species 3, was prepared by Brown and co-workers from the flash vacuum photolysis of phthalic anhydride.[71] It is possible that a small amount of this molecule could be formed during the sublimation of BDA, and that an additional quantity would be formed upon photolysis. The enhancement of the 1793 cm^{-1} peak upon annealing agrees with the work done by Radziszewski et al on the photolysis of phthalic anhydride.[75] Attempts were made to perform this experiment at lower sublimation temperatures and thus at lower concentrations of BDA. This should serve to reduce dimer formation. It was possible to identify the precursor 1811 cm^{-1} band and to observe the formation of CO_2 upon photolysis. However, the overall concentrations of photolysis products were too low to allow the observation of new bands. Thus it was not possible to determine if the 1793 cm^{-1} peak was in fact absent. The assignment of this band must remain tentative.

Figure 5-11 shows the spectrum of BDA in krypton, before and after photolysis. Figure 5-12 shows the analogous experiment in neon. Other than a slight matrix shift, krypton matrix experiment yields results identical

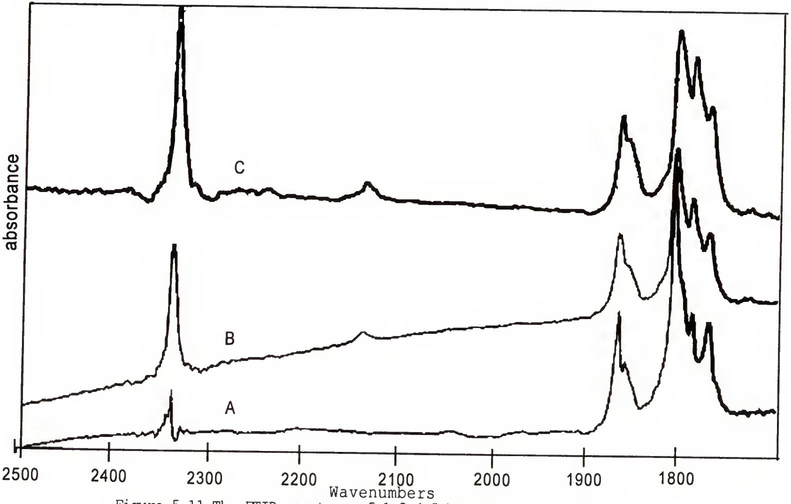

Figure 5-11 The FTIR spectrum of 1,2,4,5-benzenetetracarboxylic dianhydride in solid krypton. A)Original sample. B)After photolysis C)Following annealing to 32K.

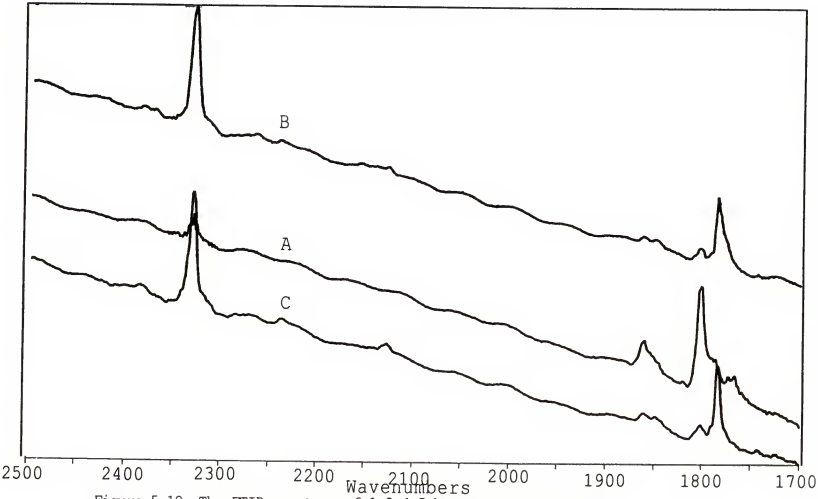

Figure 5-12 The FTIR spectrum of 1,2,4,5-benzenetetracarboxylic dianhydride in solid neon. A)Original sample. B)After photolysis C)Following annealing to 6K.

to argon. The neon matrix spectrum shows significant differences. By comparison to the results presented in reference 73, and references therein, the neon matrix seems to favor the formation of species 4, which is a cyclopropenone derivative, over species 2. This species results in a band at 1859cm^{-1} in argon[73] and is seen here as a shoulder at 1860cm^{-1}. Moriyama et al[73] report this as an intermediate between BDA and species 2, the photolysis time, 45 minutes, is identical for the krypton and neon matrices shown.

CHAPTER 6
MATRIX ISOLATION FT-RAMAN SPECTROSCOPY

Introduction

Raman spectroscopy is able to provide information about vibrational modes that are not accessible through infrared spectroscopy; however, the development of this technique as applied to matrix isolation has been slow and problematic. The Raman effect, as described earlier, is much less intense than many of the phenomena that can occur in a molecule upon excitation with an intense light source. Competing processes that are observed include fluorescence and Raleigh scattering. The lack of sensitivity and the frequency of interference have prevented Raman spectroscopy from enjoying the widespread use and rapid technical advances of infrared absorption.

The challenges of using conventional light sources limited Raman spectroscopy to being a difficult research technique. The need for intense monochromatic light has been met by the expanding availability of laser technology. This has allowed the development of commercial instruments that can be used for routine analysis. While Raman spectroscopy has traditionally used visible light, one recent advance has been the use of near-infrared (NIR) excitation in Raman spectroscopy. Shifting the excitation source to a lower energy significantly reduces the likelihood of fluorescent interference and the problems of sample heating. However, since the intensity of Raman scattering decreases with a ν^4 dependence,[76] the shift in excitation frequency must be carefully examined. Some samples will absorb NIR radiation, and as with any change in excitation frequency, care must be taken in interpretation of any resulting resonant effects. In addition to the most important advantage of decreased fluorescence, NIR excitation has allowed the coupling of interferometry and Fourier transform techniques to Raman spectroscopy.

Fourier transform Raman spectroscopy (FT-Raman) has the same advantages over conventional instruments realized by its infrared counterpart years earlier.[77] In both infrared and Raman spectroscopy the following advantages of interferometry over dispersive measurements are realized. The first is the high wavenumber accuracy of an interferometer. Known as the Connes advantage, this allows for easy and accurate signal averaging of multiple scans.[78] If the signal to noise ratio (SNR) of the spectrum is limited by detector noise it will improve with the square root of the number of scans averaged.[79] This can provide a means of observing weak bands in a spectrum. The second benefit is the multiplex or Fellgett's advantage.[80] This results from the fact that all frequencies of the spectrum are measured simultaneously. Thus for a given measurement time the intensity of light detected is much greater. Fellgett's advantage will be lost if the SNR of the instrument is shot noise limited.[79] This is generally the case for the photomultiplier detectors used in the visible spectral region, reducing the benefits of interferometry for these measurements. The third advantage is the increased throughput available from exchanging the small slit aperture of a dispersive instrument to the circular light path of an interferometer. This is known the Jacquinot advantage.[81]

All of these benefits are realized through the use of a device called an interferometer. The most widely used form of this device is the Michelson interferometer, the basic design of which is shown in figure 6-1. This device consists of one fixed and one moveable mirror separated by a beam splitter. In addition, a compensator is required to correct for the width and refractive index of the beam splitter.[79] Light from the excitation source is directed onto a beam splitter which transmits one half of the radiation through to the fixed mirror over a distance L, while reflecting the remaining light to the movable mirror.

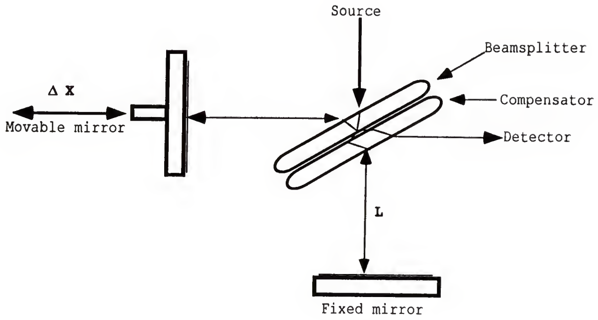

Figure 6-1 The Michelson interferometer.

As the position of the movable mirror is changed the path length traveled by the two light waves will differ by $2\Delta X$. The light is then recombined and will interfere in a constructive manner giving an intensity maximum if the pathlength difference is an exact multiple of the wavelength. A minimum will be observed if the difference in pathlength is an odd multiple of $\lambda/2$. The resulting pattern detected is known as an interferogram. The interference pattern generated from a monochromatic source such as a helium neon laser takes the form of a sinusoidal wave given by equation 1.

$$I(x) = S(\bar{\nu})\ \cos(2\pi\bar{\nu}x) \qquad (1)$$

Where $I(x)$ is the intensity of light observed and $S(\bar{\nu})$ is the intensity of the source light at that wavenumber. The interferogram of polychromatic light is a convolution of many waves of this general form with differing frequencies and intensities. The resulting interferogram gives the intensity of light dependent on elapsed time as measured by mirror displacement. After obtaining and signal averaging the desired number of scans, the signal can be changed into a frequency dependent spectrum using a method known as a Fourier transform.[82] This process separates the individual frequency components contributing to the observed interferogram. Figure 6-2 shows an interferogram resulting

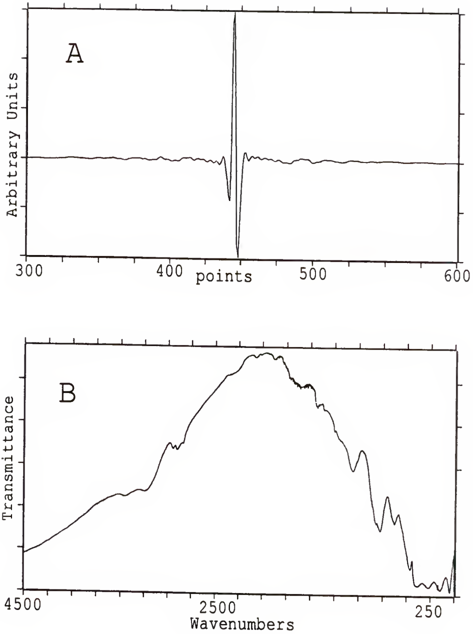

Figure 6-2 The interferogram (A) and resulting transformed spectrum (B) of a polychromatic light source.

from a polychromatic source and the resulting transformed spectrum. The interference pattern of a helium neon laser is sampled simultaneously to provide a real time frequency calibration for the overall interferogram. The signal processing algorithms involved in this transformation are well documented and beyond the scope of this work. The reader is referred to one of the several detailed texts available.[81,82]

There are several reasons to consider the adaptation of a NIR FT-Raman spectrometer for use with matrix isolation. The need for Raman data to complete the structural determination of many reactive species already partially characterized using FTIR spectroscopy is acute. Since the nature of a matrix isolation experiment allows multiple scans to be run over an extended time period for signal averaging, FT techniques would be especially useful aids in detecting weak Raman bands. The problems with fluorescence and photodecomposition that have seriously hampered visible excitation matrix Raman experiments should be reduced.

General Apparatus

In an attempt to realize the benefits described above, a matrix isolation apparatus was developed for use with a NIR FT-Raman instrument. A side view of the general apparatus is shown in Figure 6-3. This was modified for a

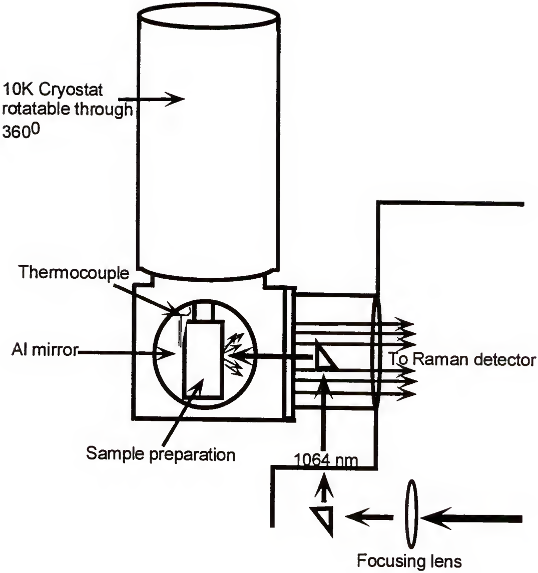

Figure 6-3 FT-Raman cryostat, side veiw.

series of experiments by using slightly different means of sample introduction, the details of which will be described later. Cooling to approximately 10K was accomplished using an APD cryogenics displex closed-cycle refrigeration system. Temperatures were monitored using two 0.07% gold in iron versus chromel thermocouples, attached at different positions on the deposition surface. A 25 watt ribbon heater provided access to higher controlled temperatures. The system was pumped to a vacuum in the range of 10^{-7} torr using a oil diffusion pump backed up by a mechanical fore pump. Samples were usually deposited on a highly polished aluminum mirror, although some runs were made overlaying this surface with silver foil. The cryostat allowed the rotation of the surface to different positions for sample deposition and the measurement of spectra.

All spectra were obtained using a Bruker FRA106 Raman accessory attached to a Bruker IFS66 NIR FTIR spectrometer. The instrument contains two non-standard options important to this application. The first is a more powerful 6 watt water cooled continuous beam neodymium: yttrium aluminum garnet (Nd:YAG) laser. The second is an optional extended range liquid nitrogen cooled germanium detector. The 180^0 excitation geometry shown in figure 6-3 was used for all samples, with spectra scanned through a 3mm thick pyrex window mounted at the front flange of the cryostat. All spectra were taken at 2 cm^{-1} resolution.

Individual Experiment Setup and Results

The setup proved immediately successful in allowing the measurement of FT-Raman spectra of stable molecules in a matrix environment. Gaseous samples were introduced neat or premixed with the matrix gas through a copper inlet tube directed toward the deposition surface. The distance from the inlet tube to the deposition surface was varied and optimized at approximately 3cm. Deposition was performed at pressures in the range of 10^{-5} to 10^{-6} torr and for times ranging from 30 minutes to several hours depending on the mixture concentration and matrix gas. Spectra were also obtained for nitrogen/argon and methane/argon systems at varying concentrations. The spectrum of 0.1% cyanogen in argon is shown in figure 6-4.

After successfully obtaining spectra of stable precursor molecules, an attempt was made to use ultraviolet photolysis and corona discharge methods to create radicals and less stable isomers of the parent compounds. Initially, the corona discharge technique was used to irradiate a cyanogen (Matheson) in argon (Airco 99.999%) mixture as described in Chapter 3 for use in conjunction with the FTIR spectra of this system. This resulted in the formation of

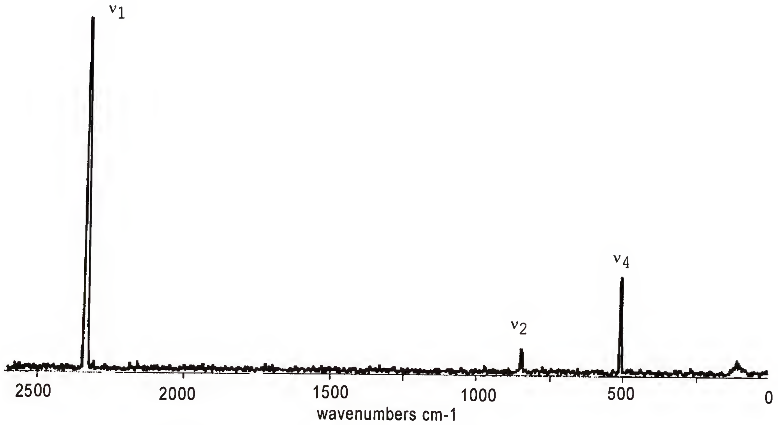

Figure 6-4 FT-Raman spectrum of 0.1% cyanogen in solid krypton.

what appeared to be a fluorescent background, rendering Raman measurements impossible. The discharge experiment was then repeated using only argon, giving less intense but comparable structure. The FT-Raman spectrum of the sample surface was taken after evaporation of the matrix and showed no residual signal. Deposition of argon through the apparatus without using the discharge also resulted in a clean background. It was then assumed that the observed fluorescence was a result of the photolysis of some impurity present in the system and a systematic elimination of causes was begun. Possible sources of impurities included something present in the argon initially, by-products of the greases and oils used in the vacuum system and contamination due to sputtering from the apparatus. These were all investigated.

The first approach was to vary the matrix gas. Krypton was corona discharged, giving similar results, as did a 1:1 molar mixture of argon and krypton. Fearing contamination through sample handling, new samples of argon and krypton were obtained and deposited directly from the original cylinders, but no change was observed. The addition of an oxygen binding catalyst in line with the system appears to reduce but not entirely eliminate the observed peaks. The use of nitrogen and xenon as matrix gases provided a different but strongly fluorescent background. Examples of these spectra can be seen in figures 6-5, 6-6 and 6-7.

In hopes that the effect seen could be reduced through annealing, the temperature dependence of this unknown species was investigated. The effect was seen to increase upon warming, and while decreasing somewhat with re-cooling, still remained in greater intensity than initially present. In order to realize a decrease in the phenomenon sufficient heating was required to visibly decrease the amount of matrix material present. Figure 6-8 shows a temperature study of corona discharged krypton. Previous investigators have found limited success in reducing fluorescence in Raman samples through bleaching the sample with the excitation source. Extended exposure to the instruments Nd:YAG laser caused an increase in the observed spectrum, likely due to local heating of the matrix.

The effect of the deposition surface on the fluorescent background was also investigated. The contamination of the aluminum block by the grinding compound used to polish it was investigated by depositing on the unpolished back surface. When this proved unsuccessful, the aluminum block was overlaid with 99.999% pure silver foil obtained from Aesar. Deposition on this surface gave comparable results.

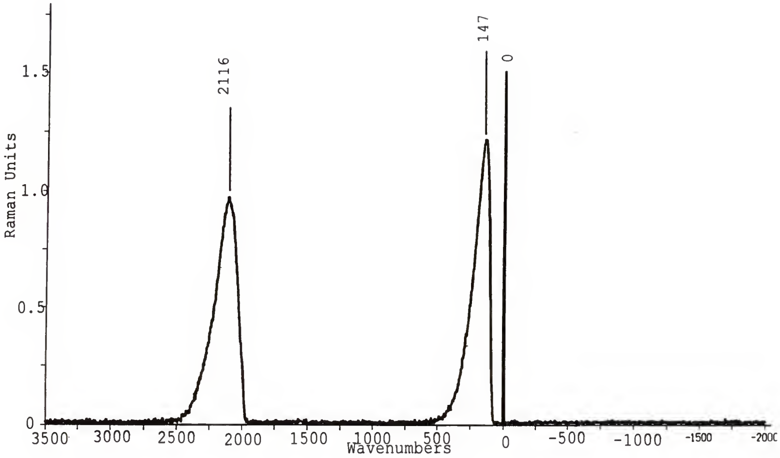

Figure 6-5 Spectrum of an argon matrix with trace impurities deposited with vacuum UV photolysis.

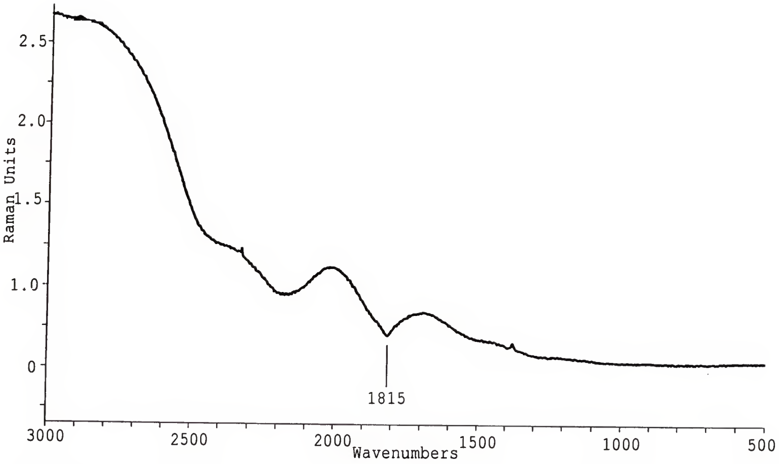

Figure 6-6 The spectrum of nitrogen containing trace impurities following photolysis with vacuum UV radiation.

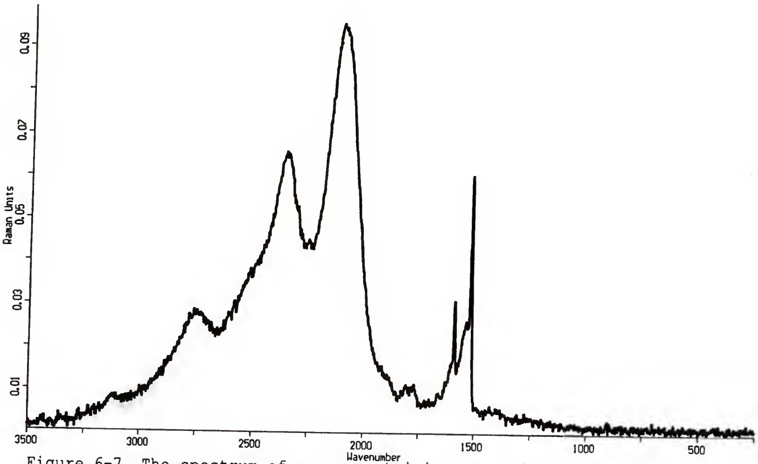

Figure 6-7 The spectrum of xenon containing trace impurities including oxygen, following photolysis with vacuum UV radiation.

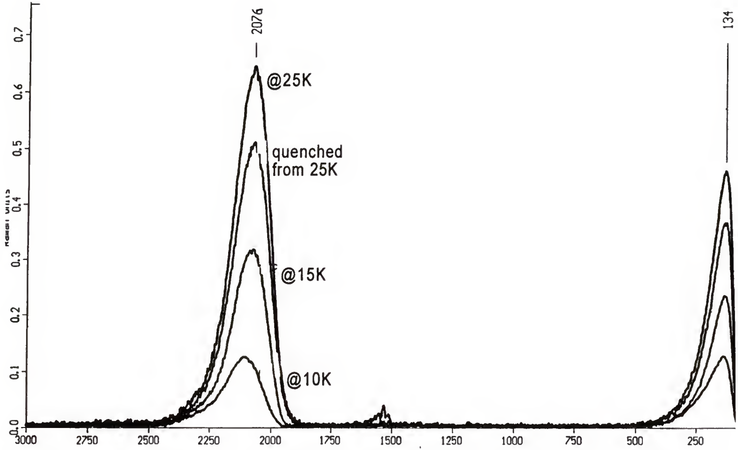

Figure 6-8 The effects of temperature on the spectrum of a krypton matrix containing trace impurities.

One other possible source of contamination was the sputtering of impurities from the corona discharge apparatus. Since the wire filament of the corona is noticeably sputtered onto the walls of the glass capillary, it was examined first. The filament was changed from tungsten to molybdenum wire. This did not prove effective. In case these metals, which are manufactured by a similar process, contained a common impurity a third change to platinum wire was performed. This also caused no change in the spectrum observed. The possibility that the quartz capillary might contain some species which could be desorbed during discharge was considered and a new corona was manufactured using a higher grade quartz known as suprasil (Englehard). To further eliminate variables from the system, this new apparatus was made completely of quartz, removing the previously described nylon connectors (see Chapter 3). None of these changes proved helpful.

Since transition metal atoms are known to be NIR fluorescent, the sputtering of these species from the flanges used to attach the corona apparatus to the cryostat was a possible interference. A series of changes were tried to eliminate this as a cause. The first was to change the original brass flanges for a larger throated model made from stainless steal. This provided a more inert material at a larger distance from the discharge. When this did not cause any change, the discharge was shielded inside first a Pyrex then Teflon sleeve. These measures also failed.

While the above-mentioned experiments were taking place several other issues were addressed. These involved the chance of contamination from the greases and oils necessary to maintain the vacuum system. Several refinements were made to the system to minimize the back-diffusion of oils into the sample chamber. A liquid nitrogen trap was added above the oil diffusion pump. The effluent used in this pump was changed from a hydrocarbon based (Santovac-5) diffusion pump oil to a silicone pump fluid (Dow Corning 704). The grease used in conduction with the flange o-rings was also changed from hydrocarbon to silicon. The o-ring material was varied from Viton to Teflon to eliminate this as a possible source. None of these changes had an impact on the spectra obtained.

The focus of the investigation had by now shifted towards the identification of the species responsible for these persistent fluorescence bands. After eliminating the apparatus as a probable cause of the observed spectrum, the possibility of trace atmospheric gases in the vacuum system was investigated. While there appeared to be no evidence of the Raman shifts of species such as nitrogen and carbon dioxide in the matrices scanned, the efficiency of fluorescence is many times that of scattering phenomena. It would therefore be possible to observe fluorescent by-products of the photolysis of a parent species that was not present in great enough concentration to give an observable Raman spectrum.

In the corona discharge, the rare gas being excited in the discharge is condensed to form the matrix so that any impurities or radicals formed in that process are trapped in the solid and observed in the Raman spectrum. An alternative approach is to utilize only the ultraviolet radiation to irradiate the matrix gas (perhaps containing the precursor molecule) as it is being considered. This is made possible by the windowed microwave discharge tube shown in figure 6-9. The windows used with this system were either lithium fluoride (LiF) or magnesium fluoride (MgF_2). While LiF transmits at higher energy, it is more hydgroscopic and forms color centers, thus requiring frequent annealing and repolishing. An argon plasma was chosen for its high energy (11.6 electron volts) and low cost. The gas was excited to a plasma inside the air-cooled quartz tube with a Raytheon microwave power generator. The argon pressure was maintained at pressures less than 1 torr by constant pumping with a mechanical fore pump. This

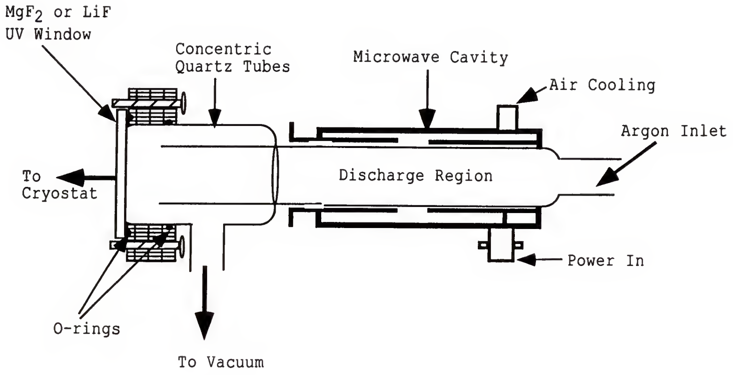

Figure 6-9 Windowed microwave discharge tube.

intense source of vacuum ultraviolet radiation was found to reproduce the results obtained using corona discharge excitation.

Several important features of this system had emerged. The fluorescence occurs following photolysis of the "pure" rare gas (or the rare gas containing the molecule to be dissociated). The emission signal intensity increases upon annealing of the matrix, and the resulting bands are both broad and have no resolvable sharp features. The line shapes and positions argon and krypton matrices (see figure 6-5 and 6-8), while nitrogen and xenon yield different and considerably broader bands that contain some coarse structure (figures 6-6 and 6-7).

Experiments were now performed by introducing known quantities of suspected impurities into the system. Samples containing 0.1%-1% oxygen (Airco, 99.99%) dissolved in argon and in krypton produced very strong fluorescence bands of the type seen earlier. It had been noted that the use of an oxygen binding catalyst appears to reduce the intensity of these signals. It was observed that the observed spectrum possesses several bands surrounding the previously identified Raman shift for the symmetric stretch of molecular oxygen in solid argon reported by Andrews and coworkers.[83] The previous work used visible excitation and it is known that the observed structure of Raman bands can change drastically with excitation frequency.[77]

Discussion

The spectrum of 0.1% O_2 in krypton is shown in figure 6-10. This was observed to be several orders of magnitude more intense than would be predicted for conventional spontaneous Raman scattering. If the energy of the excitation source lies at or near an electronic transition for the molecule a process called resonance Raman will be observed. Resonant excitation can enhance observed Raman modes by as much as 5 orders of magnitude.[36] The Nd:YAG laser falls at an energy of 9,399 cm^{-1}. The difference between the v=1 vibrational level of the $^1\Delta_g$ excited state and the v=0 level of the $^3\Sigma_g$ oxygen ground state is known to be 9400 cm^{-1}.[84] While this is a parity forbidden transition, it can still contribute to the resonance Raman effect if the influence of the matrix disturbs the symmetry of the states. The $^1\Delta_g$ has been observed to have a very long lifetime, which is significantly affected by the matrix gas.[85] The resonance effect changes the observed scattering dramatically as the excitation source is scanned into an absorption peak,[86] making the interpretation of a single excitation wavelength difficult. While the instrument used in this work is limited to a single excitation energy, there

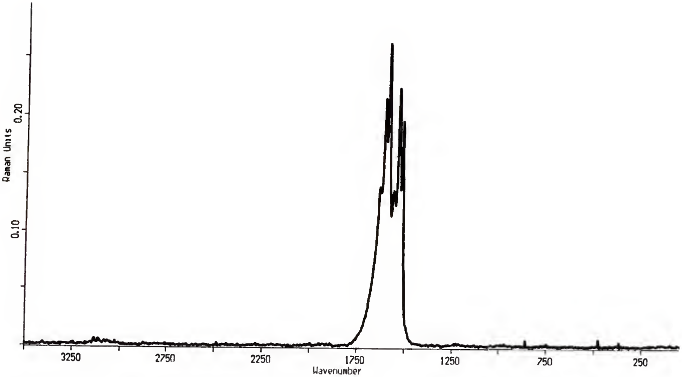

Figure 6-10 The spectrum of 0.1% oxygen in solid krypton at 12K.

has been previous work done by other groups using visible excitation.[87-90]

Figure 6-11 shows the comparison of the resonance Raman bands of 0.1% oxygen in argon and krypton matrices. This spectrum is quite complicated when compared to the single peak at 1553 cm^{-1} observed previously for argon matrix excited with 15mW of 488 nm radiation signal averaged over 70 minutes,[90] or at 1551 cm^{-1} as seen with 514.5 nm excitation.[87] These are quoted for 1% oxygen in argon. The interpretation of these bands is complicated by the large number of states available to the molecule under the conditions of this experiment.

There are a large number of effects that can be observed in resonance Raman spectra. In addition to the progression corresponding to the vibrations of the ground state, progressions originating from excited electronic states are frequently observd.[91-95] Resonance Raman transitions excited through metastable states have also been reported.[96] Electronic resonance Raman and two photon processes are also accessible. All of these different types of lines are often seen to be split into multiple components.[93] The oxygen spectrum shown in figures 6-10, 6-11 and 6-12, are difficult to interpret because they contain

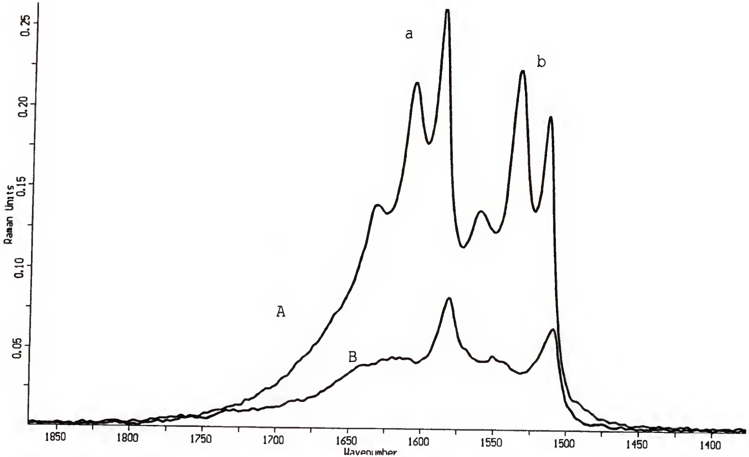

Figure 6-11 The comparison of 0.1% oxygen in solid krypton (A), to 0.1% oxygen in solid argon (B). Both spectra are taken at 12K.

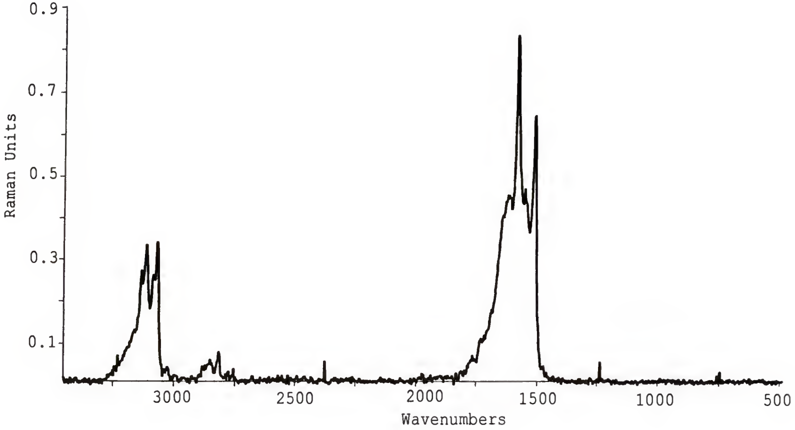

Figure 6-12 The spectrum of 1% oxygen in solid argon at 12K.

contributions from at least two of the aforementioned effects. The small frequency range accessible to this instrument further complicates the assignment of these features. Since the vibrational energy level spacing of the two lowest lying electronic states of oxygen is known to be on the order of 1500 wavenumbers,[84] only two members of the resonance Raman progressions will be observable using this detector. If the series of bands between 1500 and 1750cm^{-1} is assumed to result from the v″=0 to v″=1 transitions then the weaker band progression observed at 3000 - 3250cm^{-1} can be attributed to a v″=0 to v″=2 transition.

There appear to be two main groups of bands within each of the aforementioned regions. These are labeled **a** and **b** in figure 6-11. One possible assignment would be to attribute each group to vibrational transitions originating within different electronic state. The **b** group provides a nice match to the ground state parameters. After the molecule decays from the excited state, there are significant populations in higher level ground vibrational levels, v″=1,2,3… There are three components shown here. If the 1561cm^{-1} band were assigned to the v″=0 to v″=1 transition, then the 1535cm^{-1} band would correspond to the v″=1 to v=2 transition and the 1515cm^{-1} would then be the v″=3 to v″=2 transition. These transitions occur at an energy spacing equal to approximately $2\omega_e x_e$. This pattern and proposed assignment is seen in several matrix isolation metal dimer resonance Raman spectra.[92,93,97,98]

It is difficult to determine even a tentative assignment for band **a**. If these components were part of an excited state resonance Raman band, they would be expected to fall at lower frequency than the ground vibrational state band. While it is possible to identify what may be an overtone in the spectrum of 1% O_2 in argon (figure 6-8, 3000 - 3250cm^{-1}), other members of this progression would not fall within the spectral region observable in this experiment. It is important to compare the relative intensities of overtone bands in order to distinguish between phenomena such as resonance fluorescence and resonance Raman.[99] The width of the bands seen in these spectra suggest that they may result from fluorescence processes. While these two processes can be differentiated by scanning the excitation frequency, it is not possible with the existing instrument. A resonance Raman band would always fall at the same shift from the excitation source, while a fluorescence band would not. The limited spectral range available for investigation coupled with the large spacing of overtone bands prevent any definite assignments from being made within these spectra.

The microwave discharge of Ar-O_2 mixtures has been used to produce matrix isolated ozone.[99,100] The production of ozone using UV photolysis has also been reported.[101] The presence of ozone as an impurity in our samples following photolysis must be suspected. As a test of this, ozone-noble gas mixtures were prepared according to the procedure developed by Spiker and Andrews.[102] These mixtures were deposited at several concentrations, ranging from 0.1% to 5% O_3 in both argon and krypton. An FT-Raman spectrum of ozone was not obtained from any of these samples. The 1064nm excitation appears to cause the dissociation of ozone, as evidenced by the appearance of the oxygen spectra identical to those described earlier.

Ozone is known to have several low-lying electronic states which absorb in the near infrared.[103-107] Anderson and Mauersberger have obtained absorption spectra of ozone which show several overlapping bands at and around the energy of the Nd:YAG laser. These bands are attributed to long lived triplet states which are commonly referred to as the Wulf absorption bands.[104] In this case, these are being excited through the ν_2 bending fundamental mode.[103] Ozone is known to have a dissociation energy of 1.04 eV or 8388 cm^{-1} in the gas phase.[103] The Nd:YAG laser (9399cm^{-1}) is of sufficient energy to cause dissociation, however the stabilization of

O_3 by an argon matrix has been reported.[72] Using an argon ion laser for excitation at 5145 and 4880Å, Andrews and Spiker observe a considerable increase in the lifetime of ozone.[72] Since the Nd:YAG laser energy falls within an absorption band of a dissociative state,[103] it is likely that it is particularly efficient in causing decomposition.

The experimental evidence indicates that "pure" argon and krypton, when excited by ultraviolet light from the corona or microwave discharge, produce a molecule which fluoresces at 10K when irradiated by the 1064nm laser light. The molecule is quite stable in the rare-gas matrices at low temperatures, and appears to increase in concentration during annealing. Since each of these gases contain small percentages (0.0005%) of O_2 one suspects that O_3 is formed during the discharge, but this was ruled out as the fluorescent species as discussed above. Since water is also often a contaminant in our vacuum system, it is possible that the emitting species contain hydrogen and oxygen, e.g., HO_2. This is the present hypothesis which is being pursued.

CHAPTER 7
ELECTRON SPIN RESONANCE THEORY

Introduction

If an atom or molecule possesses a permanent magnetic moment μ, it can be studied through its interaction with an applied magnetic field **H**. Systems that are paramagnetic, i.e. those which contain at least one unpaired electron, possess a net electronic angular momentum and meet this requirement. The technique of electron spin resonance or ESR uses the application of an oscillating magnetic field with fixed frequency electromagnetic radiation to induce resonant absorptions corresponding to transitions between the Zeeman levels of paramagnetic systems. ESR has provided valuable information about molecular structure and the chemical properties of systems ranging from crystal lattice defects and radicals to conducting polymers.

This chapter will begin by providing an overview of the theory necessary to interpret ESR spectra. This description will be limited to results of direct application to the spectra of Na_2^+ to be presented subsequently. The reader is encouraged to refer to references 108-117 for a more complete treatment.

Atomic Interactions in a Magnetic Field.

The simplest case, where a magnetic dipole μ, provided by an unpaired electron, is placed in an applied magnetic field **H**, yields a Hamiltonian operator

$$H = -\mu \bullet \mathbf{H} \tag{1}$$

The overall magnetic dipole moment contains contributions from its orbital angular momentum $\mathbf{P}_L$ and also from its intrinsic angular momentum $\mathbf{P}_S$, as shown in equations 2 and 3.

$$\mu_L = -\frac{e}{2mc}\mathbf{P}_L \tag{2}$$

$$\mu_s = 2\left(-\frac{e}{2mc}\right)\mathbf{P}_S \tag{3}$$

While classical physics does not place any orientation constraints on μ and H, quantum mechanics requires that the angle θ between them be quantized. Thus, if J is assigned as the quantum number to represent the total angular momentum, the system will have 2J+1 allowed orientations, i.e., with values ranging from J to -J. Likewise, the expressions shown in equations 2 and 3 must be replaced with their quantum mechanical counterparts. Analogous to

J, The component quantum number L is assigned to orbital angular momentum and gives energy levels denoted as m_L. The spin angular momentum quantum number S, results in m_S which takes on values between S and -S. It is useful to define the quantity β_e as the Bohr magneton with a value of 9.2741 x 10^{-21} or $\left(\frac{eh}{4\pi mc}\text{ joules}/_{\text{gauss}}\right)$. Then $g_e\beta$ is substituted into equation 3, where g_e= 2.002319304386(20) is the electron g factor. This factor diverges from the 2 shown in equation 3 due to quantum mechanical considerations.

The preceding information can be used to derive expressions for the energy E of a specific quantum state. For the case of an atom with only the intrinsic electron angular momentum or spin, this is given in terms of m_s as

$$\mathrm{E}m_S = g_e \beta_e m_S H \tag{4}$$

This gives the allowed Zeeman energy levels for an atom in a magnetic field. While equation 4 holds true for a free electron, normally the electron is influenced by its atomic (or molecular) environment. For Russell-Saunders coupling of L and S, i.e. when $L \neq 0$, J can take values of L+S, L+S-1 $\ldots|L-S|$. With m_J retaining the same constraints as before, equation 4 becomes

$$Em_J = g_J \beta_e m_J H \tag{5}$$

where in an atom g_J is the Lande′ splitting factor

$$g_J = 1 + \frac{S(S+1) + J(J+1) - L(L+1)}{2J(J+1)} \tag{6}$$

In the situation of a free spin L = 0, $m_S = m_J = \pm 1/2$, and two energies are given by equation 4, $E = \pm 1/2 g\beta_e H$. Figure 7-1 shows the resulting energy levels. The transition between the Zeeman levels shown here can be excited by electromagnetic radiation of frequency ν_o at a right angle to the magnetic field.

Nuclear Hyperfine Splitting

Figure 7-1 shows the ESR signal observed for a free electron. The ESR spectrum of an atom or molecule will usually show additional splitting of energy levels resulting from the interaction of the electron with one or more nuclei. While this increases the complexity of the spectrum, it also increases the amount of information that can be obtained.

If the nucleus of an atom contains a non-zero magnetic moment or spin, the magnetic moment of the unpaired electron will interact with the nuclear magnetic moment to split the Zeeman levels into hyperfine components. The nuclear spin quantum number is I, and the resulting

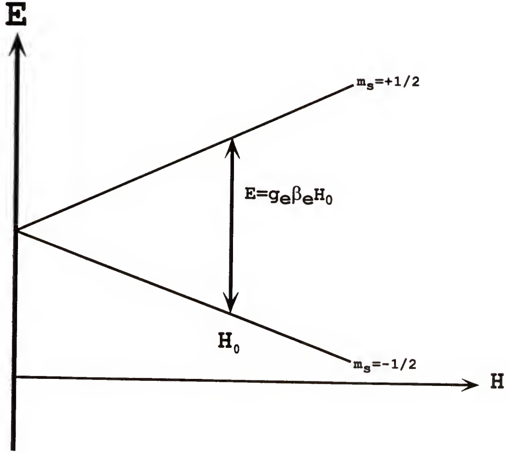

Figure 7-1 The electronic Zeman splitting observed for a free electron in a magnetic field H_0.

magnetic moment will have 2I+1 levels designated by m_I. This will split each Zeeman level into 2I+1 levels, allowing a like number of resonant transitions. Thus for an atom with I=3/2, each of the two Zeeman levels arising from the interaction of one unpaired electron with a magnetic field would be split into 4 components as shown in figure 7-2. The magnitude of these additional splitting is dependent on the nuclear magnetic moment μ_I which is characteristic of the particular element. These values are found tabulated in terms of the magnetogyric ratio $\gamma_n = \frac{\mu_I 2\pi}{Ih}$ in such references as 117.

Thus far the interaction of the electron with an external magnetic field has been described, also the influence of the nucleus on the electron was discussed. Although these are the two most important types of interactions, there is also a third consideration, which is the nuclear Zeeman interaction with the external field. This last factor is only observed at high magnetic fields and can usually be ignored. Taking these three factors into consideration, equation 1 can be rewritten to give a Hamiltonian expression for an atom in a magnetic field.

$$H = g_J \beta_e \mathbf{H} \bullet \mathbf{J} + hA\mathbf{I} \bullet \mathbf{J} - g_I \beta_n \mathbf{H} \bullet \mathbf{I} \qquad (7)$$

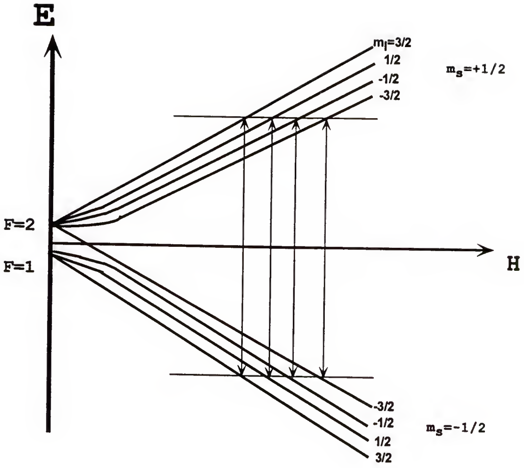

Figure 7-2 The splitting of electronic Zeeman levels observed for an I=3/2 atom.

Where g_I is the nuclear g value and β_n is the nuclear magneton. Note that the second term is independent of external fields and is hence designated the zero-field splitting factor. This term introduces A the hyperfine splitting parameter, which is a measure of the electron-nuclear interaction discussed above.

Figures 7-1 and 7-2 show that the splitting of the electronic Zeeman levels varies with the strength of the magnetic field. The magnitude of the splitting caused by the applied field relative to the hyperfine splitting has important consequences for the interpretation of the observed spectrum. The system to be discussed in this work was interrogated within a magnetic field that created a Zeeman splitting of the same order of magnitude as the hyperfine splitting. Under these conditions, m_J and m_I are coupled to give $m = m_J + m_I$. Since **I** and **J** are no longer independent, they must be replaced with the quantum number **F** = **I** + **J**. The resulting energy levels can then be interpreted using the Breit-Rabi equation,[118] shown here for J=1/2.

$$W(\mathrm{F},\mathrm{m}) = \frac{-\Delta W}{2(2\mathrm{I}+1)} - \left(\frac{\mu_\mathrm{I}}{\mathrm{I}}\right)\mathbf{H}\mathrm{m} \pm \frac{\Delta W}{2}\left(1 + \frac{4\mathrm{m}}{2\mathrm{I}+1}\mathrm{x} + \mathrm{x}^2\right)^{\frac{1}{2}} \qquad (9)$$

where $\Delta W = h(A/2)(2I+1)$ and $x=[(g_J\beta_e-(\mu_I/I))/\Delta W]\mathbf{H}$. ΔW is the energy level spacing under zero field conditions.

The interpretation of ESR spectra requires an understanding of the selection rules involved. The transitions observed arise from changes in magnetic dipole moments, this requires that only one spin, either that of the nucleus or that of the electron, flip at once. Thus if $\Delta m_j=\pm 1$,then $\Delta m_I=0$ or if $\Delta m_I=\pm 1$, $\Delta m_J=0$. ESR deals with the first case.

There are two types of interactions contributing to the observed hyperfine splitting. The first arises from the magnetic field produced by the spinning electron as seen by the nucleus. This is known as the contact or Fermi interaction.[117] Since only s electrons have a significant electron density at the nucleus, this effect gives a measure of the s character of the total spin density. The electron density at the nucleus is given as $|\psi(0)|^2$. This can be determined either experimentally or through theoretical calculations. Since s orbitals contain no angular dependence, this effect is isotropic and the contribution to the overall observed hyperfine splitting will be called A_{iso}. This can be written as

$$A_{iso} = \frac{8\pi}{3h} g_e \beta_e g_1 \beta_n |\psi(0)|^2 \qquad (10)$$

The observed A = A_{iso} + A_{dip}. The second term, A_{dip} gives the contribution caused by interactions with p and d electrons. It is the perturbation caused by the dipole moment of the electron interacting with that of the nucleus. The angular dependence of this effect results in an anisotropic interaction. This can be quantified as

$$A_{dip} = \frac{g_e g_1 \beta_e L(L+1)}{hJ(J+1)} \langle r^{-3} \rangle \qquad (11)$$

where r is the distance between the two magnetic dipoles. Note that for L=0, (i.e. an s electron) A_{dip} becomes zero.

The Effect of Molecular Orientation

The angular dependence of the magnetic parameters described earlier causes the ESR spectrum to be dependent upon the orientation of the molecule with respect to the magnetic field. The molecules to be studied in this work are contained in a solid matrix at random orientations relative to the magnetic field. Since Na_2^+ is linear, it possesses axial symmetry. Because of this departure from spherical symmetry, g and A become second rank tensors, which can be broken into parallel and perpendicular components, corresponding to the orientation of the z axis of the molecule relative to the applied magnetic field. While this effectively doubles the number of allowed transitions, the perpendicular lines are much more easily observed. This is to be expected due to symmetry considerations involving the possible orientations of the magnetic dipole of the molecule in the magnetic field. A linear molecule will have an infinite number of orientations perpendicular to the z-axis, but only 2 parallel to it.

The tensor g is anisotropic due to coupling to the orbital angular momentum of nucleus causing a divergence from the free electron value g_e. By separating out the value of g_e, a measure of the spin-orbit coupling can be measured using $\Delta g = g - g_e$. This factor can then be taken into account by the use of perturbation theory. The effects of spin-orbit coupling can be seen in the second order term of the resulting equation. This is given by

$$g = g_e \mathbf{1} + 2\lambda\Lambda \tag{12}$$

where

$$\Lambda = \sum_n \frac{\langle G|L|n\rangle\langle n|L|G\rangle}{E_n^{(o)} - E_G^{(o)}} \tag{13}$$

where G is the ground state, n is over the excited states and $E^{(o)}$ is the zero order energy of an individual state. A more complete description of this result can be found in references 119 and 120. Important results obtained by this perturbation method include expressions for $\Delta g_{\parallel}$ and $\Delta g_{\perp}$.

$$\Delta g_{/\!/} = -\tfrac{1}{2}\sum_{n} \frac{\langle n|\xi L|G\rangle^2}{E_n - E_o} \tag{14}$$

$$\Delta g_{\perp} = -2\sum_{n} \frac{\langle n|\xi L_x|G\rangle\langle G|L_x|n\rangle}{E_n - E_o} \tag{15}$$

where ξ is the molecular spin-orbit coupling constant.

The symmetry of the molecule will limit the states involved in spin-orbit coupling. This work deals with a linear homonuclear diatomic in the $^2\Sigma$ ground state. In order for the direct product of the ground state, excited state and the angular momentum operator to contain the totally symmetric representation of this symmetry group, only Π excited states can couple to the Σ ground state.

As with g, the A tensor for axially symmetric molecules can be broken into perpendicular and parallel components. These can then be related to A_{iso} and A_{dip} as shown below.

$$A_{dip} = \frac{A_{/\!/} - A_{\perp}}{3} \tag{15}$$

$$A_{iso} = \frac{A_{/\!/} + 2A_{\perp}}{3} \tag{16}$$

Since the same perturbation method described for g earlier can be used to obtain experimental values for $A_{\parallel}$ and $A_{\perp}$, these expressions prove very useful. Once values for A_{dip} and A_{iso} have been found, they can be used to construct a linear combination of atomic orbitals (LCAO) or molecular orbital (MO) description of the system of interest. This process will be demonstrated for the results presented in this work.

It is also possible to obtain an exact solution for the eigenvalues of the spin Hamiltonian. This route gives much better results than the second order perturbation method when dealing with transitions occurring at energies of comparable order to the magnetic field. While this procedure involves solving rather large matrices, it has been greatly facilitated by the use of computers. A sample calculation using the appropriate Hamiltonian will be shown later. The results obtained will then be compared to the perturbation treatment of the same data.

CHAPTER 8
SODIUM DIMER CATION

Introduction

The focus of this research is to synthesize Na_2^+ and to obtain its ESR spectrum. While there has been extensive theoretical work done on the ions of alkali metal dimers,[121-125] experimental work is limited to photo-dissociation experiments. The ionization potentials and bond strengths of Na_2^+ have been determined through optical-optical double resonance spectroscopy on the Rydberg states of the neutral clusters.[127-129] Photodepletion spectroscopy has provided a direct probe of Na_2^+, yielding a dissociation energy of 0.991±0.001eV.[130] Further experimental work on the ions remains limited.[131] While the role of hyperfine structure of individual sodium atoms on cluster formation has been studied via associative ionization of laser-cooled sodium,[132] there have been no previously reported values for the molecular hyperfine structure.

Theoretical investigations have primarily concentrated on high lying excited states and on larger alkali metal clusters and ions. Mulliken electronic populations are available only at the uncorrelated unrestricted Hartree-Fock level, and predict that the unpaired electron will be evenly shared between the two sodium nuclei.[124] This calculation predicts the unpaired electron has exclusively s character, in contrast to our findings. Among the higher level *ab initio* calculations performed on this system,[123-125] work by Bonacic-Kountecky et al. is particularly interesting.[126] In addition to calculating a bond length for this molecule of 3.536±0.003Å, attention is paid to the difference in energy between the ground $^2\Sigma_g$ state and the $^2\Pi_u$ excited state. This quantity is calculated to be 3.03eV. This is in good agreement with the experimental value of 3.05eV obtained by Ellert et al.[131]

Experimental

The Na_2^+ molecule was matrix isolated as described in Chapter 1. For this experiment, cryogenic temperatures were obtained using an Air Products Heli-Tran dewar, which supplies a continuous flow of liquid helium. This provides an operating range of 4-300K. The addition of a rotary pump on the boil off vent allowed temperatures as low as 1.8K to be reached. A schematic representation of this apparatus is shown in figure 8-1. This system was maintained under vacuum using a 4 inch turbo molecular pump

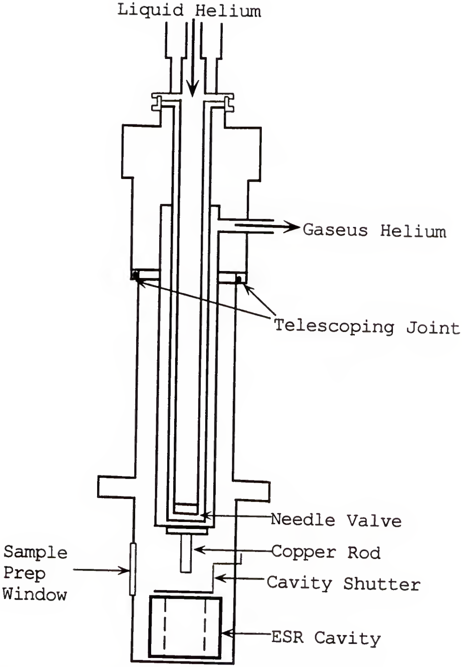

Figure 8-1 ESR cryostat, side-view schematic.

manufactured by Varian. When backed up by a mechanical pump, this provided a 300 liter per second pumping speed. The base pressure for this apparatus was on the order of 10^{-6} torr, which could be attained in approximately 2 hours.

The sample matrix was deposited on both sides of a 32 x 2.9 x 0.7 mm copper rod. This is screwed into the Heli-Tran apparatus with an indium o-ring providing good thermal contact. The temperature of the rod was monitored using a chromel vs. Au-0.02 atom % Fe thermocouple placed at the junction between the rod and cryostat. A 20 watt heater was also placed at the tip of the cryostat to allow warming of the apparatus for sample changing.

One important feature of the apparatus shown in figure 8-1 is the telescoping joint. This allows the copper rod to be raised out of the ESR cavity for sample deposition. The sample preparation area can be isolated from the cavity by a shutter to avoid contamination. A thin-walled quartz tube is also used to line the cavity for this same reason. Samples are prepared with the rod in the upper position, then a pneumatic lift is used to lower the matrix into the ESR cavity to obtain spectra.

The sample preparation area is accessible from three sides, with the fourth being joined to the vacuum system.

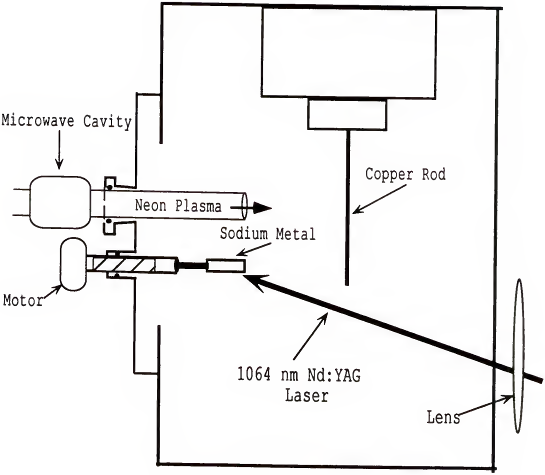

Figure 8-2 Sample preparation area, side-view cross-section.

Figure 8-2 shows the arrangement used in these experiments. The matrix gas used was neon (Linde, 99.998% purity). Sodium metal (Aldrich, 99.9%) was vaporized using the 1064nm fundamental of a pulsed Q-switched Nd:YAG laser. Co-excitation was provided by a 2450 MHz microwave discharge (16.8eV neon resonance emission). The plasma was generated using the same procedure outlined in Chapter 6, using the discharge tube shown in figure 6-9; however, in this case the microwave plasma was vented into the deposition chamber, providing the matrix gas. Sample deposition occurred over a 30 minute period. During this time the Na rod was rotated using a small motor to provide a more uniform deposition. After 15 minutes the copper rod was turned 180^0 to allow even coating of both sides. The temperature was maintained at 4K throughout the experiment. Following sample deposition, the cavity shutter was opened and the copper rod coated with matrix was lowered into the ESR cavity to obtain spectra. The entire cavity was then placed between the poles of the magnet. All electron spin resonance measurements were made at X-band (approximately 9.6 GHz) frequencies, using a klystron and Bruker ER 200D SRC spectrometer.

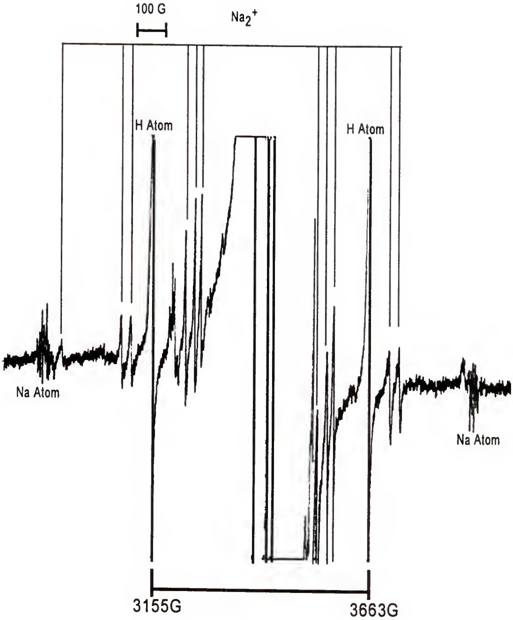

Figure 8-3 The ESR spectrum of Na_2^+in solid neon.

Results

The ESR spectrum of Na_2^+ is shown in figure 8-3. Also seen are signals resulting from sodium atoms, H atoms and some unidentifiable signals at g = 2. The lines observed span from about 2500 to 3800 G. Assuming two equivalent nuclei with I = 3/2, this allows J to take on values of 0, 1, 2 and 3. This will result in m_J ranging from +J to -J in each case. The large hyperfine interaction in Na_2^+ causes splitting of lines which would normally overlap. Thus J=0 gives one line at the g of the molecule. J=1 will give three lines which fall at g plus a second order term which varies with M_J,[117] correspondingly, J=3 will result in 7 lines. There are a total of 32 predicted lines including both perpendicular and parallel contributions. However, only 23 assignments can be made due to interference at g = 2, and overlap of Na atom lines at high field. Figure 8-4 shows an expanded view of two regions of the Na_2^+ spectrum.

The perpendicular lines as indicated in table 8-1 were fit by obtaining the eigenvalues generated by the appropriate spin Hamiltonian for this system, which is given in equation 1.[133]

$$\hat{\mathrm{H}} = \mathrm{g}_{\parallel}\beta H_z S_z + \mathrm{g}_{\perp}\beta(H_x S_x + H_y S_y) + \mathrm{A}_{\parallel} J_z \mathrm{S}_z + \mathrm{A}_{\perp}\beta(J_x S_x + J_y S_y) \qquad (1)$$

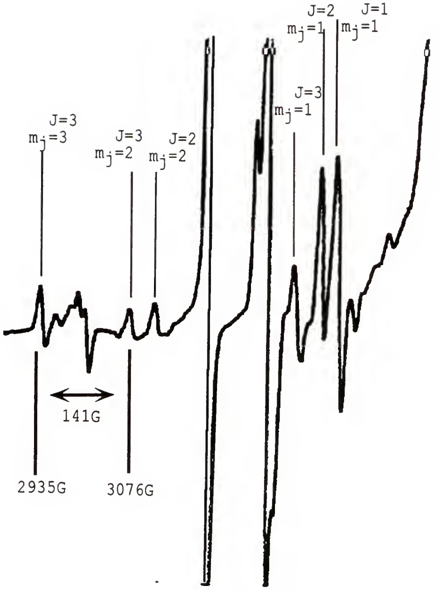

Figure 8-4 Expanded view of Na_2^+ in argon showing low field perpendicular lines.

Table 8-1 The observed line positions of the ESR spectrum of Na_2^+ in solid neon compared to the calculated values.

J, m_j	$H_\perp$ obs ±1G	$H_\perp$ calc G	$H_\parallel$ obs G	$H_\parallel$ calc G
3,3	2935.0	2935.1	2947.9	2949.9
3,2	3075.5	3075.7	3084.1	3085.7
2,2	3099.9	3101.6	3106.2	3107.8
3,1	3222.5	3222.0	3227.5	3228.6
2,1	3245.0	3245.3	3249.2	3249.8
1,1	3259.8	3260.5	3266.2	3267.0
3,0	3378.0	3378.1		3378.4
2,0		3400.2		3400.4
1,0	3414.3	3414.5		3415.0
0,0		3421.2		3420.9
3,-1	3539.4	3538.8		3535.4
2,-1	3561.6	3561.4	3558.5	3558.2
1,-1	3576.5	3576.8	3573.8	3574.1
3,-2	3709.3	3709.2	3701.7	3700.6
2,-2	3731.9	3732.6	3725.0	3725.1
3,-3		3884.0		3875.7

To evaluate $H_\perp$ or $H_{||}$ a matrix of the order (2S + 1) (2J + 1) = 2(2J + 1) must be solved, where J = $|I_1 + I_2|, \ldots |I_1 - I_2|$ and M_j = J, J-1, …-J. Since S = 1/2, M_s ±1/2. The spin matrix was set up individually for each I value. Figure 8-5 shows the spin matrix for I=3, S=1/2. This 14x14 matrix is symmetric, so only the diagonal and upper half need be considered. The matrix is set up as indicated in figure 8-5 and the non-zero elements are listed in table 8-2. A suitable fit was generated by carefully varying the magnetic parameters $A_\perp$ and $A_{||}$; and then comparing the calculated to the observed perpendicular line positions. Once values for these parameters were obtained, the parallel line positions were calculated. By considering the phase and relative intensities, the observed parallel lines were assigned, and are also given in table 8-1.

It is also possible to obtain values for $A_\perp$ and $A_{||}$ using the second order perturbation method. By solving equation 2 simultaneously for a sufficient number of lines, these parameters can be generated. A set of example calculations is shown in the Appendix.

$$H = H_0 - A_\perp m_J - \frac{A_{//}^2 A_\perp^2}{4H_0}\left[I(I+1) - m_J^2\right] \qquad (2)$$

m_s m_j	½ 3	½ 2	−½ 3	½ 1	−½ 2	½ 0	−½ 1	½ −1	−½ 0	½ −2	−½ −1	½ −3	−½ −2	−½ −3
½ 3	1	2	4	7	11	16	22	29	37	46	56	67	79	92
½ 2		3	5	8	12	17	23	30	38	47	57	68	80	93
−½ 3			6	9	13	18	24	31	39	48	58	69	81	94
½ 1				10	14	19	25	32	40	49	59	70	82	95
−½ 2					15	20	26	33	41	50	60	71	83	96
½ 0						21	27	34	42	51	61	72	84	97
−½ 1							28	35	43	52	62	73	85	98
½ −1								36	44	53	53	74	86	99
−½ 0									45	54	64	75	87	100
½ −2										55	65	76	88	101
½ −1											66	77	89	102
½ −3												78	90	103
½ −2													91	104
½ −3														105

Figure 8-5 The spin matrix for I=3, S=1/2. The non-zero elements obtained are given in table 8-2.

Table 8-2 Non-zero spin matrix elements numbered as indicated in figure 8-5.

Matrix element and value	Matrix element and value
BH(1)=0.5DO*C +1.5DO*$A_{\parallel}$	BH(42)=BH(4)
BH(3)=0.5DO*C+$A_{\parallel}$	BH(44)=BH(27)
BH(4)=0.5DO*S	BH(45)=-0.5D0*C
BH(5)=1.2247448714*$A_{\perp}$	BH(55)=0.5D0*C-$A_{\parallel}$
BH(6)=-0.5DO*C-1.5DO*$A_{\parallel}$	BH(63)=BH(4)
BH(10)=0.5DO*C+1.5DO*$A_{\parallel}$	BH(65)=BH(14)
BH(12)=BH(4)	BH(66)=-0.5DO*C+0.5DO*$A_{\parallel}$
BH(14)=1.5811388301*$A_{\perp}$	BH(78)=0.5DO*C-1.5DO*$A_{\parallel}$
BH(15)=-0.5DO*C-$A_{\parallel}$	BH(88)=BH(4)
BH(21)=0.5DO*C	BH(90)=BH(5)
BH(25)=BH(4)	BH(91)=-0.5DO*C+$A_{\parallel}$
BH(27)=1.7320508076*$A_{\perp}$	BH(103)=BH(4)
BH(28)=-0.5DO*C-0.5DO*$A_{\parallel}$	BH(105)=-0.5DO*C+1.5DO*$A_{\parallel}$
BH(36)=0.5DO*C-1.5DO*$A_{\parallel}$	

DO = zero field splitting
S = $G_{\perp}$*B*Dsinθ/2.0023
C = $G_{\parallel}$*B*Dcosθ/2.0023
All other variables as previously defined.

This is usually not sufficiently accurate in treating transitions occurring at energies near that of the applied magnetic field. When this treatment was applied to the observed lines shown in table 8-1, a value of $A_\perp$ of 158.4(5)MHz is found, as compares to 158.4(9)MHz obtained using the exact equation. $A_\parallel$ is found to be 164.8MHz vs. the 154.9MHz given by equation 1. Equation 2 yields the energy level diagram for Na_2^+ as shown in figure 8-6.

Analysis

The derived magnetic parameters are collected in table 8-3. With this information the extent of the spin orbit mixing of p electronic character into the ground s state can be determined. Values for A_{iso} and A_{dip} were calculated from $A_\perp$ and $A_\parallel$ as described in Chapter 7. Since A_{dip}=-3.27 MHz the hyperfine splitting is not entirely isotropic. This anisotropy can be attributed in a first approximation to pσ character in the ground state. A theoretical value for A_{iso} can be obtained by combining literature values for the neutral atom with that of Na^+.[117,134] By assuming A_{dip} for a pσ state to be 1/40 of A_{iso}, the theoretical value for A_{dip} of 23G can be derived. These values are calculated assuming that all spin density is contained in the sσ

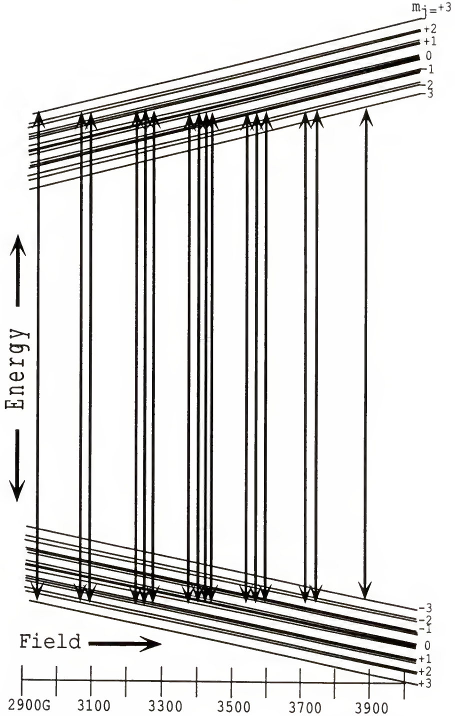

Figure 8-6 Energy level diagram for perpendicular ESR transitions of Na_2^+. Arrows indicate predicted ESR transitions, while lines represent the energy levels involved.

Table 8-3 Derived magnetic parameters for Na_2^+ in solid neon at 4K.

Derived parameter	
$g_{\parallel}$	2.0006(9)
$g_{\perp}$	2.0017(9)
$A_{\parallel}$	154.9(9)G 434.1 MHz
$A_{\perp}$	158.4(9)G 443.9 MHz
A_{iso} (MHz)	obs. 440.6 MHz theo. 1387. MHz
A_{dip} (MHz)	obs. -3.27 MHz theo. -23 MHz
$\left|\psi^\circ\right|^2$ (au)	0.3725
$\left|\left\langle 3\cos^2\theta - 1/r^3\right\rangle\right|$ (au)	0.04632
%$\tilde{s}$	63.5%
%$p\sigma$	28.4%

state, so comparison with the observed parameters allows the estimation of the percent p character in the state. $2A_{dip}$ for Na_2^+ is 6.54 MHz, which when taken with the theoretical value, yields a pσ contribution of 28%. It is necessary to take twice A_{dip} to account for the nuclear dilution between the two Na atoms. An analogous treatment of A_{iso} yields a %sσ character of 64%. Thus accounting for all of the spin.

The observed shift in $g_\perp$ ($\Delta g_\perp = g_\perp - g_e$) allows calculation of the energy difference between the Σ ground state and nearest Π excited state.[133]

$$\Delta g_\perp = (2\xi / \Delta E)\langle \Pi | L_x | \Sigma \rangle \langle \Sigma | L_x | \Pi \rangle \qquad (2)$$

Using equation 2, and substituting in a spin-orbit coupling constant for the sodium atom, $\xi = 11.46\ \mathrm{cm}^{-1}$, ΔE is found to be 11,000 cm^{-1}. This can be compared to the energy difference of the Na atom at 16,973.4 cm^{-1}.[134] Since the sign of $\Delta g_\perp$ is negative, the $^2\Pi_r$ state is the lowest available excited state, and has the properties of an electron in a π orbital.[117]

In addition to comparing Na_2^+ to the sodium atom, comparison can be made to the Na_3 molecule. The sodium trimer was investigated with ESR by Lindsay et al.[135] Na_3

was found to have two equivalent sodium atoms, with further analysis yielding isosceles triangle geometry. The unpaired spin density was concentrated on the equivalent atoms, and was seen to have predominately s character. One possible bonding mechanism for this molecule is an ionic combination of Na_2^+…Na. This molecule yields a seven-line hyperfine splitting pattern. It gives a g value of 2.0012 and values of A_{iso} = 150G and A_{dip} = 23G.

It would be interesting to compare Na_2^+ to the dimer cations of other alkali metals. Unfortunately, there is very little information on these species. There have been no reported ESR spectra of these molecules. There are theoretical treatments of Li_2^+ and K_2^+.[121-125, 136] The bond energy of Li_2^+ has been investigated using optical-optical double resonance spectroscopy,[128] giving $10464 \pm 6 cm^{-1}$ or eV. This can be compared to 0.986ev for Na_2^+.[84]

CHAPTER 9
CONCLUSIONS

A novel synthesis of C_2N_2 dimers was developed using the corona discharge of cyanogen in argon. This allowed the formation of isocyanogen and diisocyanogen with very few interfering byproducts. After obtaining the FTIR spectrum of this system for three different isotopomers, normal coordinate analysis was used to calculate force constants for isocyanogen. The *ab initio* calculations coupled with the observed isotopic shifts allowed the identification of the ν_3 stretching vibration of diisocyanogen.

The infrared spectra of two didehydrogenated polycyclic aromatic hydrocarbons were obtained. The spectra of 1,2-naphthyne and 2,3-naphthyne were observed in neon, argon and krypton matrices. The observed spectra were assigned through comparison with theoretically calculated line positions and intensities, and also with each other. While the benzyne analog of these systems has been studied extensively, this work represents the first infrared characterization of a larger “yne” aromatic derivative. Attempts were made to synthesis a doubly-didehydrogenated derivative of benzene, but they proved unsuccessful.

In order to allow further characterization of the systems studied here using FTIR spectroscopy, matrix isolation was coupled with FT-Raman spectroscopy. This apparatus proved very successful in obtaining the matrix FT-Raman spectra of stable molecules. Problems with trace contaminates makes the use of matrix FT-Raman spectroscopy with molecules produced using UV photolysis very challenging. This instrument has been shown to be inappropriate for use in studying oxygen or ozone, but shows promise in other applications.

The X-band ESR spectrum of the sodium dimer cation was obtained in solid neon, establishing that it has a $^2\Sigma$ ground state. Both parallel and perpendicular lines could be identified for this linear molecule, allowing the exact calculation of the energy level diagram for the hyperfine splitting of the Zeeman levels. It is found that the unpaired electron has about 28% pσ character, in contrast with a theoretical calculation.

APPENDIX
A SECOND ORDER PERTURBATION TREATMENT OF Na_2^+

The second order perturbation method as described in Chapter 7 allows one to determine approximate values for the hyperfine splitting parameters $A_\perp$ and $A_{||}$. Also values for $g_\perp$ and $g_{||}$ can be found. Equation 2 from Chapter 8 is restated here:

$$H = H_0 - A_\perp m_J - \frac{A_{//}^2 A_\perp^2}{4H_0}\left[I(I+1) - m_J^2\right] \qquad (1)$$

Substitution of the observed value H for a specific line will yield a linearly independent equation for each ESR line. The line for I=3, m_J=2 is observed at 3075.5G. The transition for I=3, M_J=-2 falls at 3709.3G. Solving equation 1 for zero, and plugging in the quantities above gives

$$0 = -3075.5 + H_0 - 2A_\perp - \frac{A_{//}^2 A_\perp^2}{4H_0}\left[3(4) - 2^2\right] \qquad (2)$$

$$0 = -3709.3 + H_0 + 2A_\perp - \frac{A_{//}^2 A_\perp^2}{4H_0}\left[3(4) - (-2)^2\right] \qquad (3)$$

taking the difference of these two equations yields $A_\perp$=158.45MHz. If the sum of these two equations is taken, the result is then given in terms of H_0 and the second order term from equation 1. By writing expressions such as equations 2 and 3 for the observed ESR lines for I=3, $M_J=\pm 1$. Then, taking the sum of these two lines gives

$$3392.4G + 2H_0 - (8)\frac{A_{//}^2 A_{\perp}^2}{4H_0} = 0 \qquad (4)$$

When this is set equal to the sum between equations 2 and 3:

$$6784.8G + 2H_0 - (16)\frac{A_{//}^2 A_{\perp}^2}{4H_0} = 0 \qquad (5)$$

It can be solved for the second order term as shown in equation 6.

$$\frac{A_{//}^2 A_{\perp}^2}{4H_0} = 3.8167 \qquad (6)$$

This can then be used to obtain a value for H_0 when it is plugged into either equation 4 or 5. When taken with equation 4, H_0 is found to be 3422.9G. Returning this value into equation 6 with the already determined value for $A_\perp$, allows $A_{||}$. This was found to be 164.8MHz.

REFERENCES

1. Whittle, E.; Dows, D.A. and Pimentel, G.C., *J. Chem Phys.* **1954**, 22, 1943.

2. Gruen, D.M. *Cryochemistry;* Moscovitz, M. and Ozin, G.A. eds., Wiley, New York, **1976**, 441.

3. Weltner, W., Jr. *Science*, **1967**, 155, 155.

4. Weltner, W., Jr. *Advances in High Temperature Chemistry;* Vol. 2, Eyring, L. ed., Academic Press, New York, **1970**, 85.

5. Milligan, D. and Jacox, M.E. *MTP International Review of Science, Physical Chemistry, series I;* Vol. 3, Ramsey, D.A. ed., Butterworth, London, **1972**, 1.

7. Andrews, L. Vibrational *Spectra and Structure;* Vol. 4, Durig, J.R. ed., Elsevier, New York, **1975**, 1.

8. Pimentel, G.C. *New Synth. Methods*, **1975**, 3, 21.

9. Clark, R.J.H. and Hester, R.E. eds., *Spectroscopy of Matrix Isolated Species*, John Wiley and Sons, New York, **1989**.

10. Ball, D.W.; Kafafi, Z.H.; Fredin, L.; Hauge, R.H. and Margrave, J.L. eds., *A Bibliography of Matrix Isolation*, Rice University Press, Houston, **1988**.

11. Andrews, L. and Moscovitz, M. eds., *Chemistry and Physics of Matrix-Isolated Species*, Elsevier, New York, **1989**.

12. Jodl, H.J. *Vibrational Spectra and Structure;* Vol 13, **1984**, 285.

13. Hanna, M.W. *Quantum Mechanics in Chemistry, 2nd ed.*, W.A. Benjamin, Inc, New York, **1965**.

14. Levine, I.N. *Quantum Chemistry*, 4th ed., Prentice-Hall, Inc., New Jersey, **1991**.

15. Lowe, J.P.; *Quantum Chemistry, 2nd ed.*, Academic Press, Inc., San Diego, CA, **1993**.

16. Steinfeld, J.I. *Molecules and Radiation, an Introduction to Modern Molecular Spectroscopy*, MIT Press, Cambridge MA, **1986**.

17. Bernath, P.F. *Spectra of Atoms and Molecules*, Oxford University Press, New York, **1995**.

18. Wilson, E.B.; Decius, J.C.; Cross, P.C. *Molecular Vibrations, The Theory of Infrared and Raman Vibrational Spectra*, Dover, New York, **1955**.

19. Cotton, F.A. *Chemical Applications of Group Theory, 3rd ed,* John Wiley and Sons, New York, **1990**.

20. Herzburg, G. *Molecular Spectra and Molecular Structure: Infrared and Raman Spectra of Polyatomic Molecules,* D. van Nostrand Company, Inc., New York, **1945**.

21. Stroh, F.; Winnewisser, B.P.; Winnewisser, M.; Reisenauer, H.P.; Maier, G.; Goede, S.J. and Bickelhaupt, F., *Chem Phys Lett.*, 160, **1989**, 105.

22. Yamada, M.T.; Markus, M.W.; Winnewisser, G.; Joentgen,W.; Kock, R.; Vogel, E.; Altenbach, H.J., *Chem Phys Lett.,* 160, **1989**, 113.

23. Maier, G.; Reisenauer, H.P.; Eckwert, J.; Sierakowski, C.; Stumpf, T., *Angew. Chem. Int. Ed. Engl.,* 31, **1992**, 1218.

24. Engleking, P.C. *Rev. Sci. Instrum,* 57, **1986**, 2274.

25. Janz, G.C. *Inorganic Synthesis, Vol V;* Moeller, T., ed., McGraw-Hill, New York, **1957**.

26. Bai, H. and Ault, B.S. *Chem. Phys. Lett.* 188, **1992**, 126.

27. Williams, A.P.; Ph.D. Thesis, University of Florida, **1997**.

28. Hedburg, L.; Mills, I.M., *J. Molec. Spec.,* 160, **1993**, 117.

29. Gaussian 94, Revision B.2, Frisch, M.J.; Trucks, G.W.; Schlegel, H.B.; Gill, P.M.W.; Johnson, B.G.; Robb, M.A.; Cheeseman, J.R.; Keith, T.; Petersson, G.A.; Montgomery, J. A.; Raghavachari,K.; Al-Laham, M.A.; Zakrzewski, V.G.; Ortiz, J.V.; Foresman, J.B.; Peng, C.Y.; Ayala, P.Y.; Chen, W.; Wong, M.W.; Andres, J.L.; Replogle, E.S.; Gompeerts, R.; Martin, R.L.; Fox, D.J.; Binkley, J.S.; Defrees, D.J.; Baker, J.; Stewart, J.P.; Head-Gordon, M.; Gonzalez, C.; and Pople, J.A.; Gaussian, Inc., Pittsburgh PA, 1995.

30. Haese, N.N. and Woods, R.C. *J. Chem. Phys.,* 73, **1980**, 4521.

31. Sana, M. and Leroy, G. *J.Mol.Struct. (Theochem)*76, **1981**, 259.

32. Nguyen, M.T.; *Chem Phys Lett.,* 157, **1989**, 430.

33. Bickelhaupt, F.M.; Nibbering, N.M.M.; Van Wezenbeek, E.M. and Baerends, E.J., *J. Phys. Chem.*, 96, **1992**, 4864.

34. Botschwina, P., *J. Phys. Chem.*, 99, **1993**, 6217.

35. Atkins, P.W., *Physical Chemistry, 5th ed.*, W.H. Freeman, New York, **1994**.

36. Diem, M., *Introduction to Modern Vibrational Spectroscopy;* John Wiley and sons, New York, **1993**.

37. Wilson, E.B., *J. Chem. Phys.*, 76, **1940**, 76.

38. Meister, A.G. and Cleveland, F.F.; *Amer. J. Phys*, 14, **1946**, 13.

39. Ferigle, S.M. and Meister, A.G.; *J. Chem. Phys.*, 19, **1951**, 982.

40. Allamandola, L.J., Tielens, A.G. and Barker, J.R. *Ap. J. Letters*, 290, **1985**, L25.

41. Leger, A. and Puget, J.L. *Astron. Astrophys.*, 13, **1993**, 473.

42. Szczepanski, J.; Vala, M.; Talbi, D.; Parisel, O. and Ellinger, Y., *J. Chem. Phys.*, 96, **1993**, 4494.

43. Duley, W.W. and Williams, D.A., *MNRAS*, 196, **1981**, 269.

44. Allamandola, L.J.; Tielens, A.G.G.M. and Barker, J.R., *Astrophys. J. Lett.*, 290, **1985**, L25.

45. Pauzat, F.; Talbi, D. and Ellinger, Y., *Astron. Astrophy.*, 293, **1995**, 263.

46. Szczepanski, J.; Roser, D.; Personette, W., Eyring, M.; Pellow, R. and Vala, M., *J. Phys. Chem.*, 96, **1992**, 7876.

47. Szczepanski, J.; Vala, M.; Talbi, D.; Parisel, O. and Ellinger, Y., *J. Chem. Phys.*, 98, **1993**, 4494

48. Szczepanski, J. and Vala, M., *Nature*, 363, **1993**, 699.

49. Hudgins, D.M.; Sanford, S.A. and Allamandola, L.J., *J. Chem. Phys.*, 89, **1994**, 4243.

50. Chapman, O.L.; Mattes, K.; McIntosh, C.L. and Pacansky, J., *J. Am. Chem. Soc.*, 95, **1973**, 6134.

51. Dunkin, I.R. and MacDonald, J.G., *J. Chem. Soc., Chem. Commun.*, **1979**, 772.

52. Porter, G. and Steinfeld, J.I., *J. Chem. Soc. A*, **1968**, 877.

53. Chapman, O.L.; Chang, C.C.; Kolc, J. Rosenquist, N. R. and Tomioka, H., *J. Am. Chem. Soc.*, 97, **1975**, 6586.

54. Nam, H.H. and Leroi, G.E., *Spectrochimica Acta,* 41A, **1985**, 67.

55. Nam, H.H. and Leroi, G.E., *J. Molc. Structure*, 157, **1983**, 301.

56. Pauzat, F., Talbi, D. and Ellinger, Y., *Astron. Astrophys,* 293, **1995**, 263.

57. Weimer, H.A.; McFarland, B.J.; Li, S. and Weltner, W. Jr., *J. Phys. Chem.* 99, **1995**, 1824.

58. Campbell, A.D. and Grimmett, M.R., *Aust. J. Chem.*, 16, **1963**, 854.

59. Lohmann, J., *J. Chem.Soc., Faraday Trans. I*, 68, **1972**, 814.

60. Radziszewski, J.G.; Hess, B.A. Jr. and Zahradnik, R., *J. Am. Chem. Soc.*, 114, **1992**, 52.

61. Pauzat, F.; Talbi, D.; Miller, M.D.; DeFrees, D.J. and Ellinger, Y., *J. Phys. Chem.*, 96, **1992**, 7882.

62. Person, W.B.; Szczepaniak, K.; Szczesniak, M. and Del Bene, J.E., In *Recent Experimental and Computational Advances in Molecular Spectroscopy*, Fausto, R. Ed., Kluwer Academic Publishers, Dordrecht, **1993**, 141.

63. Scheiner, A.C. and Schaefer, H.F. III, *Chem. Phys. Lett.*, 177, **1991**, 471.

64. Liu, R.; Zhouh, X. and Pulay, P., *J. Phys. Chem.* 96, **1992**, 8336.

65. Bludsky, O.; Pirko, V.; Kobayoshi, R. and Jørgensen, P. *Chem Phys. Lett.*, 228, **1994**, 568.

66. Hobza, P.; Zahradnik, R.; Hess, B.A. Jr. and Radziszewski, J. G., *Theor. Chem. Acta*, 88, **1994**, 233.

67. Simon, J.G.G.; Münzel, N. and Schweig, A., *Chem. Phys. Lett.*, 170, **1990**, 187.

68. Scott, A.P. and Radom, L., *Chem. Phys. Lett.*, 212, **1993**, 705.

69. Brown, R.F.C.; Browne, N.R.; Coulston, K.J.; Danen, L.B.; Eastwood, F.W.; Irvine, M.J. and Pullin, A.D.E., *Tetrahedron Lett.*, 29, **1986**, 1075.

70. Wentrup, C.; Blanch, R.; Briehl, H. and Gross, G., *J. Am. Chem. Soc.*, 110, **1988**, 1874.

71. Brown, R.F.C.; Browne, N.R.; Coulston, K.J.; Eastwood, F.W.; Irvine, M.J.; Pullin, A.D.E. and Wiersom, U. E., *Aust. J. Chem.*,42, **1989**, 1321.

72. Wenthold, P.G.; Paulino, J.A. and Squires, R.R., *J. Am. Chem. Soc.*, 113, **1991**, 7414.

73. Moriyama, M.; Ohana, T. and Yabe, A., *Chem. Lett.*, **1995**, 557.

74. Moriyama, M. Ohana, T. and Yabe, A., *J. Am. Chem. Soc.* 119, **1997**, 10229.

75. Biernacki, P.R.; Kaszynski, P.; Hess, B.A.; Thulstrup, E.W. and Radziszewski, J.G., *J. Phys. Chem.* 99, **1995,** 6309.

76. Wilson, H.M.M.; Pellow-Jarman, M.V.; Bennett, B. and Hendra, P.J., *Vibrational Spectroscopy,* 10, **1996**, 89.

77. Hendra, P.J.; Jones, C. and Warnes, G., *Fourier Transform Raman Spectroscopy, Instrumentation and Chemical Applications,* Ellis Horwood, New York, **1991.**

78. Connes, J. and Connes, P., *J. Opt. Soc. Am.,* 56, **1966,** 896.

79. Griffiths, P.R. and de Haseth, J.A., *Fourier Transform Infrared Spectrometry,* Elving, P.J.; Winefordner, J.D. eds., Wiley-Interscience, New York, **1986.**

80. Felgett, P. *J. Phys. Radium,* 19, **1958**, 187.

81. Gronholz,J. and Herres, W., *Understanding FT-IR Data Processing,* Dr. Alfred Huethig Publishers, Germany, **1984.**

82. Jacquinot, P., *J. Opt. Soc. Am.,* 44, **1954**, 761.

83. Smardzewski, R.R. and Andrews, L., *J. Chem. Phys.,* 57, **1972**, 1327.

84. Huber, K.P. and Herzberg, G., *Molecular Spectra and Molecular Structure, IV. Constants of Diatomic Molecules.,* Van Nostrand Reinhold Company, New York, **1979.**

85. Crone, K.P. and Kügler, K.-J., *Chemical Physics,* 99, **1985**, 293.

86. Spiro, T.G. and Stein, P., *Ann. Rev. Phys. Chem.,* 28, **1977**, 501.

87. Kiefte, H.; Clouter, N.H.; Rich, N.H. and Ahmad, S.F., *Can. J. Phys. Vol.,* 60, **1982**, 1204.

88. Kornath, A. and Köper, I., *J. Raman Spec.,* 28, **1997**, 829.

89. Kornath, A., *J. Raman Spec.,* 28, **1997**, 9.

90. Andrews, L. and Spiker, R.C. Jr., *J. Phys. Chem.,* 76, **1972**, 3208.

91. DiLella, D.P.; Limm, W.; Lipson, R.H.; Moskovits, M. and Taylor, K.V., *J. Chem. Phys.,* 77, **1982**, 5263.

92. Moskovits, M; DiLella, D.P. and Limm, W., *J. Chem. Phys.,* 80, **1984**, 626.

93. Cosse, C.; Fouassier, M.; Mejean, T.; Tranquille, M.; DiLella, D.P. and Moskovits, M., *J. Chem. Phys.,* 73, **1980**, 6076.

94. Sontag, H.; Eberle, B. and Weber, R., *Chem. Phys.,* 80, **1983**,279.

95. Eberle, B.; Sontag, H. and Weber, R., *Chem. Phys.,* 92, **1985**, 417.

96. Moskovits, M.; Limm, W. and Mejean, T., *J. Chem. Phys.*, 82, **1985**, 4875.

97. Moskovits, M.; Limm, W. and Mejean, T., *J. Phys. Chem.*, 89, **1995**, 3886.

98. Bier, K.D.; Haslett, A.D.; Kirkwood, A.D. and Moskovits, M., *J. Chem. Phys.*, 89, **1988**, 6.

99. Andrews, L. and Spiker, R. Jr., *J. Chem. Phys.*, 59, **1973**, 1863.

100. Hopkins, A.G. and Brown, C.W., *J. Chem. Phys.*, 58, **1972**, 1776.

101. Bressler, C.G., Dyer, M.J. and Copeland, R.A., *Proceedings of the Second International Conference on Low Temperature Chemistry*, Durig, J.R. and Klabunde, K.J. eds., BkMk Press, Kansas City, **1996**, 121.

102. Spiker, R.C. Jr. and Andrews, L., *J. Chem. Phys.*, 59, **1973**, 1851.

103. Anderson, S.M. and Mauersberger, K., *J. Geophys. Res.*, 100 No.D2, **1995**, 3033.

104. Abel, B.; Charvát, A. and Deppe, S.F., *Chem. Phys. Lett.*, 277, **1997**, 347.

105. Günther, J.; Anderson, S.; Hilpert, G. and Mauersberg, K., *J. Chem. Phys.*, 108, **1998**, 5449.

106. Benderskii, A.V. and Wight, C.A.; *J. Chem. Phys.*, 104, **1996**, 85.

107. Benderskii, A.V. and Wight, C.A.; *J. Chem. Phys.*, 101, **1994**, 292.

108. Poole, C.P., Jr. *Electron Spin Resonance*, Wiley-Interscience, New York, **1967**.

109. Wertz, J.E. and Bolton, J.R. *Electron Spin Resonance: Elementary Theory and Practical Applications*, McGraw-Hill, New York, **1972**.

110. Wertz, J.E. and Bolton, J.R. *Electron Spin Resonance: Elementary Theory and Practical Applications*, Rotledge Chapman Hill, New York, **1986**.

111. Weil, J.A.; Wertz, J.E. and Bolton. J.R. *Electron Spin Resonance: Elementary Theory and Practical Applications*, Wiley-Intescience, New York, **1994**.

112. Abram, A. and Bleaney, B. *Electron Paramagnetic Resonance of Transition Ions,*Dover New York, **1986**.

113. Atkins, P.W. and Symns, M.C.R. *The Structure of Inorganic Radicals,* Elsevier, New York, **1967**.

114. Kopferman, H. *Nuclear Moments*, Academic, New York, **1962**.

115. Gordy, W. *Techniques of Chemistry Volume XV: Theory and Applications of Electron Spin Resonance;* West, W. ed. Wiley-Interscience, New York, **1980**.

116. Weltner, W., Jr. *Magnetic Atoms and Molecules,* Nostrand-Reinhold, New York, **1983**.

117. Weltner, W., Jr. *Magnetic Atoms and Molecules*, Dover, New York, **1989**.

118. Breit, G and Rabi, I. *Phys. Rev.*, 38, **1963**, 2002.

119. Stone A.J. *Proc. Roy. Soc.*, London, A271, **1963**, 424.

120. Dalgaard, E. and Linderberg, J. *J. Chem. Phys. 65,* **1967**, 692.

121. Car, R.; Meuli, R.A. and Buttet, J., *J. Chem. Phys.*, 73, **1980**, 4511.

122. Müller, W. and Meyer, W., *J. Chem. Phys.*,80, **1984**, 3311.

123. Martins, J.L.; Buttet, J. and Car, R, *Physical Review B,* 31, **1985**, 1804.

124. Spiegelmann, F. and Pavolini, D., *J. Chem. Phys.*, 89, **1988**, 4954.

125. Magnier, S.; Millié, P. Dulieu, O. and Masnou-Seeuws, F., *J. Chem. Phys.*, 98, **1993**, 7113.

126. Bonacic-Koutecký, V.; Pittner, J.; Fuchs, C.; Fantucci, P.; Guest, M.F.; and Koutecký, J., *J. Chem. Phys.*, 104, **1996**, 1427.

127. Bernheim, R.A.; Gold, L.P.; Tipton, G.T. and Konowalow, D.D., *Chem. Phys. Lett.*, 105, **1984**, 201.

128. Bernheim, R.A., Gold, L.P. and Tipton, T., 78, **1983**, 3635.

129. Bordas, C.; Labastie, P.; Chevaleyre, J. and Broyer, M., *Chem. Phys.*, 129, **1989**, 21.

130. Leutwyler, S.; Heinis, T.; Jungen, M.; Härri, H.P. and Schumacher, E., *J. Chem. Phys.*, 76, **1982**, 4280.

131. Ellert, C.; Schmidt, M.; Schmidt, C.; Reinert, T. and Haberland, H., *Phys. Rev. Lett.*, 75, **1995**, 1731.

132. Wagshul, M.E.; Helmerson, K.; Lett, P.D.; Rolston, S.L.; Phillips, W.D.; Heather, R. and Julienne, P.S., *Phys. Rev. Lett.*, 70, **1993**, 2074.

133. Goodman, B.A. and Raynor, J.B., *Adv. Inorg. Chem. And Radiochem.*, 13, **1970**, 136.

134. Moore, C.E., *Atomic Energy Levels as derived from the Analysis of Optical Spectra, Vol. 1 Circular 467*, U.S. government Printing Office, Washington D.C., **1949**, 89.

135. Lindsay, D.M.; Herschbach, D.R. and Kwiram, A.L., *Molec. Phys.*, 32, **1976**, 1199.

136. Bishop, D.M. and Puochan, C., *Chem. Phys. Lett.*, 102, **1983**, 132.

BIOGRAPHICAL SKETCH

Heather Ann Weimer was born on July 29, 1972, in Akron Ohio, to Donald D. and Susan J. Weimer. She was graduated from West Holmes Senior High School in Millersburg, Ohio, in June 1990. She was graduated from the College of Wooster in Wooster, Ohio, in May 1994 with a Bachelor of Arts in Chemistry. She conducted undergraduate research with Dr. William Weltner at the University of Florida and with Dr. David Powell at the College of Wooster. Since May of 1994 she has attended Graduate School at the University of Florida where she has pursued the degree of Doctorate of Philosophy in physical chemistry. She enjoys spending time with friends and horseback riding.

I certify that I have read this study and that in my opinion it conforms to the acceptable standards of scholarly presentation and is fully adequate, in scope and quality, as a dissertation for the degree of Doctor of Philosophy.

William Weltner, Jr.
William Weltner, Jr., Chairman
Professor of Chemistry

I certify that I have read this study and that in my opinion it conforms to the acceptable standards of scholarly presentation and is fully adequate, in scope and quality, as a dissertation for the degree of Doctor of Philosophy.

John R. Eyler
John R. Eyler
Professor of Chemistry

I certify that I have read this study and that in my opinion it conforms to the acceptable standards of scholarly presentation and is fully adequate, in scope and quality, as a dissertation for the degree of Doctor of Philosophy.

Martin Vala
Martin T. Vala
Professor of Chemistry

I certify that I have read this study and that in my opinion it conforms to the acceptable standards of scholarly presentation and is fully adequate, in scope and quality, as a dissertation for the degree of Doctor of Philosophy.

David E. Richardson
Professor of Chemistry

I certify that I have read this study and that in my opinion it conforms to the acceptable standards of scholarly presentation and is fully adequate, in scope and quality, as a dissertation for the degree of Doctor of Philosophy.

Alan M. Jacobs

Alan M. Jacobs
Professor of Nuclear
Engineering Sciences

This dissertation was submitted to the Graduate Faculty of the Department of Chemistry in the College of Liberal Arts and Sciences and to the Graduate School and was accepted in partial fulfillment of the requirements for the degree of Doctor of Philosophy.

August 1998

Dean, Graduate School